Results in Engineering 29 (2026) 108331

Contents lists available at ScienceDirect

Results in Engineering

journal homepage: www.sciencedirect.com/journal/results-in-engineering

Research paper

Qualitative dynamics and solitary wave phenomena in a new extended Boussinesq-Type KdV equation

Mehmet Şenol [a], Bahadır Kopçasız [b], Hatice Ceyda Türk [a], Homan Emadifar [c,d,*], Karim K. Ahmed [e]

[a] Nevşehir Hacı Bektaş Veli University Department of Mathematics, Nevşehir, 50300, Türkiye
[b] İstanbul Gelişim University Department of Basic Sciences, Faculty of Engineering and Architecture, İstanbul, 34310, Türkiye
[c] Department of Mathematics, Saveetha School of Engineering, Saveetha Institute of Medical and Technical Sciences, Saveetha University, Chennai postcode, Tamil Nadu, India
[d] Department of Basic Sciences, Technical and Vocational University (TVU), Tehran, Iran
[e] Department of Mathematics, Faculty of Engineering, German International University (GIU), New Administrative Capital, Cairo, Egypt

ARTICLE INFO

Keywords:
Extended KdV equation
Kumar-Malik method
Chaos analysis
Bifurcation
Sensitivity
Phase-portrait
Poincaré map
Time series

ABSTRACT

In the present study, the extended Boussinesq-type Korteweg-de Vries (KdV) equation is solved by the Kumar-Malik (KM) method to yield new families of analytical traveling-wave solutions. The model has been transformed into ordinary differential equations through suitable traveling-wave transformations, and the ODE is solved to obtain explicit solutions as Jacobi elliptic, hyperbolic, trigonometric, and exponential functions. The dynamical characteristics of these solutions are further examined via bifurcation analysis, sensitivity to initial conditions, and phase-portraits. In addition, the chaotic dynamics of the system are explored using bifurcation diagrams, Poincaré maps, and time series representations. The results demonstrate multifaceted dynamical effects, including periodic, quasi-periodic, and chaotic transitions. The study provides valuable information on the nonlinear complex processes of extended Boussinesq-type KdV models and may serve as a basis for additional theoretical and applied research.

1. Introduction

Partial differential equations form the most powerful tools in mathematical modeling to express spatial and temporal changes of such physical quantities as heat, fluid velocity, electromagnetic fields, or wave amplitudes. However, NLPDEs constitute a much more extensive and difficult class of problems that arise almost everywhere in natural applications, and linear PDEs have long been extensively discussed and well resolved. If the unknown function or its derivatives appear in a nonlinear form, such as nonlinear powers, products of derivatives, or nonlinear functions of the solution, the PDE is considered nonlinear. This nonlinearity significantly complicates both the theoretical analysis and numerical solution of the equations [1]. Such equations underpin nonlinear modeling in diverse scientific and engineering disciplines, bridging mathematical formulation with observable physical phenomena in fluids, plasmas, elasticity, and nonlinear optics.

In contrast to linear PDEs, which frequently allow superposition of solutions and can be resolved analytically through methods like separation of variables or Fourier transforms, NLPDEs typically do not have closed-form solutions and require advanced mathematical and computational tools. NLPDEs arise in many scientific and engineering fields. The Navier-Stokes equations, which are intrinsically nonlinear, govern viscous fluid motion in fluid dynamics. Einstein's field equations, which are nonlinear PDEs, describe the structure of spacetime in general relativity. From optical pulses in fiber optics (via the nonlinear Schrödinger equation) to shallow water waves (via the KdV equation), nonlinear wave equations describe a wide variety of phenomena [2,3].

Nonlinear heat equations for phase transitions, and reaction-diffusion equations for chemical reaction and biological pattern formation are some examples. Solutions for NLPDEs may have very different behaviors from solutions for their linear counterparts. Phenomena such as shock waves, turbulence, solitons, chaos, and pattern formation are possible only in NLPDEs. Solving NLPDEs is often a combination of techniques from functional analysis, dynamical systems, variational methods, and numerical approximations. In the recent past, computational methods like machine learning-based solvers, finite element, and finite volume methods have become unavoidable, especially for high-dimensional and real-time applications [4].

* Corresponding author.
E-mail addresses: msenol@nevsehir.edu.tr (M. Şenol), bkopcasiz@gelisim.edu.tr (B. Kopçasız), haticecyd@gmail.com (H.C. Türk), homan_emadi@yahoo.com (H. Emadifar), Karim.kamal.502@gmail.com (K.K. Ahmed).

https://doi.org/10.1016/j.rineng.2025.108331
Received 28 August 2025; Received in revised form 5 November 2025; Accepted 19 November 2025
Available online 27 November 2025

Among NLPDEs, the KdV equation put forward by Korteweg and de Vries [5] has been studied widely in those systems in which both dispersion and nonlinearity are dominant. Extended forms of the KdV equation, e.g., Boussinesq-type equations, have been interesting with their ability to model bidirectional wave propagation. These extended forms include higher-order derivatives and more involved nonlinear terms to model physical systems more realistically [6,7]. The Boussinesq-type KdV equation is a significant mathematical model of nonlinear wave propagation in a vast variety of physical conditions [8–10]. Within this framework, the Boussinesq and KdV-type models serve as canonical examples where nonlinearity and dispersion coexist, giving rise to solitary waves and complex propagation behaviors observed in many physical media.

Whereas a variety of analytical approaches have been employed for KdV- and Boussinesq-type equations, few studies have investigated both their analytical and qualitative dynamics within a unified framework. Most of the research focuses either on exact solutions or on numerical simulation and with less attention to the underlying bifurcation and chaotic patterns. Motivated by this gap, the present work employs the Kumar-Malik method to derive new explicit solutions of the extended Boussinesq-type KdV equation and to examine their dynamical transitions through bifurcation and chaos analyses. This integrated approach makes an original contribution to the literature by introducing soliton theory into contact with nonlinear dynamical behavior for multidimensional dispersive systems.

Numerous analytical methods have been developed to obtain exact solutions of such nonlinear wave equations. These include the extended modified rational expansion method [11,12], the improved modified Sardar sub-equation technique [13], the modified $\left(\frac{G'}{G^2}\right)$-expansion method [14], and the generalized exponential rational function (GERF) method [15–18]. Other popular approaches are the general projective Riccati equation method [19], the modified simple equation method [20], the modified Kudryashov method [21,22], the Hirota bilinear method [23], the multiple-scale method [24,25], and the Lie symmetry method [26–35]. Recent progress in the analysis of non-autonomous nonlinear evolution equations, including space- or time-dependent extensions, has revealed new classes of variable-coefficient solitons and richer dynamical behaviors [36–38]. In recent years, several studies have reported significant advances in soliton dynamics, nonlinear wave interactions, and their interdisciplinary applications in optics, fluids, and plasma systems [36,39–41]. These works demonstrate the growing interest in exploring richer nonlinear structures and serve as a motivation for the present investigation.

To the best of the authors' knowledge, the present work is the first detailed investigation of the extended Boussinesq-type KdV model following the original formulation by Wazwaz. Since no subsequent studies directly addressing this exact model have been reported in the literature, there is no prior work available for quantitative comparison. Therefore, this paper establishes a new analytical and dynamical framework for the model by applying the Kumar-Malik method and coupling it with bifurcation and chaos analyses to reveal its rich nonlinear behavior. The main objectives of this study are: (i) to derive analytical solutions using the Kumar-Malik approach, a recent and powerful technique in nonlinear wave theory [42]; (ii) to perform sensitivity and chaos analyses to examine the effects of small perturbations and transitions to chaos; and (iii) to carry out bifurcation analysis to describe the evolution from regular to chaotic dynamics.

By uniting solution techniques with nonlinear dynamical analysis, this work aims to offer a comprehensive picture of the Boussinesq-type KdV model structure and dynamics. The results make considerable contributions to the nonlinear wave equation theoretical structure and to applications in nonlinear wave equations to engineering and physics.

Wazwaz and Kaur [43] have conducted a comprehensive analysis on Boussinesq-type equations, such as:

$$\Phi_{tt} + \Phi_{xx} - \beta\Phi_{xxxx} - \lambda(\Phi_{xx})^2 + \theta\Phi_{xt} = 0, \tag{1.1}$$

$$\Phi_{tt} - \Phi_{xx} - \beta\Phi_{xxxx} - \lambda(\Phi_{xx})^2 + \theta\Phi_{xt} + \frac{\alpha^2}{4}\Phi_{yy} + \alpha\Phi_{yt} = 0, \tag{1.2}$$

$$\Phi_{tt} - \Phi_{xx} - \beta\Phi_{xxxx} - \lambda(\Phi_{xx})^2 + \theta\Phi_{xt} + \frac{\alpha^2}{4}\Phi_{yy} + \alpha\Phi_{yt} + \kappa\Phi_{xz} = 0. \tag{1.3}$$

Here, the constants $\alpha, \beta, \lambda, \theta, \kappa$ are nonzero coefficients. Eq. (1.1) corresponds to the $(1+1)$-dimensional case, Eq. (1.2) is a $(2+1)$-dimensional model with $\Phi = \Phi(x, y, t)$, and Eq. (1.3) extends to $(3+1)$-dimensions with $\Phi = \Phi(x, y, z, t)$. Wazwaz and Kaur verified the complete integrability of these equations using the Painlevé test and obtained multiple soliton solutions via the simplified Hirota method (SHM) [43].

The additional terms in these models-such as $\theta\Phi_{xt}$, $\frac{\alpha^2}{4}\Phi_{yy} + \alpha\Phi_{yt}$, and $\kappa\Phi_{xz}$-enhance the realism of wave interactions, including oblique wave collisions in surface gravity waves. Notably, the fourth-order derivative Φ_{xxxx} captures dispersion effects, while Φ_{xx} and Φ_{yy} represent dissipation [44].

From the study by Wazwaz and Kaur, a new $(3+1)$-dimensional Boussinesq-type equation was introduced:

$$\Phi_{tt} + \Phi_{xx} + \gamma\Phi_{xxxx} + \lambda(\Phi^2)_{xx} + \theta\Phi_{xy} + d\Phi_{xz} + f\Phi_{xt} = 0. \tag{1.4}$$

Eq. (1.4) describes the propagation of weakly nonlinear, weakly dispersive waves in multidimensional media where both higher-order dispersion and nonlinear effects coexist. Here, Φ denotes the wave potential (or displacement field), α characterizes the transverse perturbation strength, β represents the higher-order dispersion coefficient, λ and θ measure the quadratic and mixed-derivative nonlinearities, respectively, and κ accounts for longitudinal, transverse coupling.

In geophysics, Boussinesq-type KdV equations model tsunami and internal ocean waves. In elasticity theory, they model nonlinear stress waves with applications to seismic or man-made material phenomena. In nonlinear optics, similar equations govern the propagation of light pulses in fibers operating in soliton-like regimes.

Mathematically, such equations often have integrability characteristics and exact solutions through methods such as the inverse scattering transform, Lie symmetry analysis, or perturbative approaches. The cross-derivative terms in Eq. (1.4) describe rich multi-directional interactions and increase physical reality.

Finally, these equations are valuable points of reference in computational mathematics, making it possible to construct and verify numerical algorithms for the solution of NLPDEs. Their prevalence speaks to their inherent importance in both theoretical and applied research.

The structure of the paper is as follows: the mathematical model and the Kumar-Malik approach are presented in Section 2; analytical solutions are derived in Section 3; graphical illustrations are given in Section 4; bifurcation phenomena are analyzed through phase portraits in Section 5; chaotic dynamics and sensitivity to perturbations are investigated in Section 6; and finally, the conclusions are summarized in Section 7.

2. Mathematical model and analytical method

2.1. Traveling wave transformation

The NLPDE of the form is considered as follows:

$$P(\Phi, \Phi_x, \Phi_y, \Phi_z, \Phi_t, \Phi_{xx}, \Phi_{xy}, \Phi_{xz}, \Phi_{xt}, \ldots) = 0. \tag{2.1}$$

Here, $\Phi = \Phi(x, y, z, t)$. is the wave function. For the suggested model, apply the following traveling wave transformations to find solutions, given as

$$\Phi(x, y, z, t) = \Phi(\xi), \quad \xi = kx + ly + mz + nt, \tag{2.2}$$

where k, l, m, n is the wave speed constant, Eq. (2.1) transforms it into an ordinary differential equation (ODE):

$$O\left(\Phi, \Phi', \Phi'', \ldots\right) = 0. \tag{2.3}$$

2.2. Overview of the Kumar-Malik method

The explanation of the Kumar-Malik method is given in this subsection [45].

Phase 1. The general solution of Eq. (2.3) is described as:

$$\Phi(\xi) = A_0 + \sum_{j=1}^{N} A_j Q(\xi)^j. \tag{2.4}$$

Here, the constants A_j's $(j = 1, 2, 3, \dots, N)$ are arbitrary parameters to be found, and the function $Q(\xi)$ satisfies the first-order ODE:

$$\left[Q'(\xi)\right]^2 = \left[\rho_1 Q(\xi)^4 + \rho_2 Q(\xi)^3 + \rho_3 Q(\xi)^2 + \rho_4 Q(\xi) + \rho_5\right], \tag{2.5}$$

where ρ_1,ρ_2 ,ρ_3 ,ρ_4 and ρ_5 are arbitrary constants.

Phase 2. We apply the balance principle to Eq. (2.3) to find the value of N.

Phase 3. The coefficients of $Q^N(\xi)$ become zero when Eq. (2.4) and its derivatives, together with Eq. (2.5), are inserted into Eq. (2.3). As a result, an algebraic system of equations is produced. The soliton solutions for Eq. (2.3) are obtained by solving this system.

Phase 4. By replacing the solutions of Eq. (2.3) with Eq. (2.2), various analytical solutions of the Eq. (2.1) are achieved.

The solution to Eq. (2.5) is presented as follows:

Case 1. If $\rho_4 = \frac{\rho_2\left(4\rho_1\rho_3-\rho_2^2\right)}{8\rho_1^2}$, $\rho_5 = 0$, then we achieve the **Jacobi elliptic solutions** as follows

Sub-Case 1.1. If $\rho_1 < 0$, and $(4\rho_1\rho_3 - \rho_2^2) > 0$, then

$$Q_{1,1}(\xi) = -\frac{\rho_2}{4\rho_1} + \frac{\rho_2}{4\rho_1}\mathrm{cn}\left[\frac{\sqrt{-\rho_1(4\rho_1\rho_3-\rho_2^2)}}{2\rho_1}\xi, \frac{\rho_2}{2\sqrt{(4\rho_1\rho_3-\rho_2^2)}}\right], \tag{2.6}$$

$$Q_{1,2}(\xi) = -\frac{\rho_2}{4\rho_1} + \frac{\rho_2}{4\rho_1}\mathrm{dn}\left[\frac{\rho_2}{4\sqrt{-\rho_1}}\xi, \frac{2\sqrt{(4\rho_1\rho_3-\rho_2^2)}}{\rho_2}\right]. \tag{2.7}$$

Sub-Case 1.2. If $\rho_1 < 0$, $(4\rho_1\rho_3 - \rho_2^2) < 0$, and $(16\rho_1\rho_3 - 5\rho_2^2) < 0$, then

$$Q_{1,3}(\xi) = -\frac{\rho_2}{4\rho_1} + \frac{\sqrt{-(16\rho_1\rho_3-5\rho_2^2)}}{4\rho_1} \mathrm{cn}\left[\frac{\sqrt{(4\rho_1\rho_3-\rho_2^2)\rho_1}}{2\rho_1}\xi, \frac{2\sqrt{(4\rho_1\rho_3-\rho_2^2)(16\rho_1\rho_3-5\rho_2^2)}}{2(4\rho_1\rho_3-\rho_2^2)}\right], \tag{2.8}$$

$$Q_{1,4}(\xi) = -\frac{\rho_2}{4\rho_1} + \frac{\sqrt{-(16\rho_1\rho_3-5\rho_2^2)}}{4\rho_1} \mathrm{dn}\left[\frac{\sqrt{(4\rho_1\rho_3-\rho_2^2)\rho_2}}{4\rho_1}\xi, \frac{2\sqrt{(4\rho_1\rho_3-\rho_2^2)(16\rho_1\rho_3-5\rho_2^2)}}{16\rho_1\rho_3-5\rho_2^2}\right]. \tag{2.9}$$

Sub-Case 1.3. If $\rho_1 < 0$, $(4\rho_1\rho_3 - \rho_2^2) > 0$, and $(16\rho_1\rho_3 - 5\rho_2^2) < 0$, then

$$Q_{1,5}(\xi) = -\frac{\rho_2}{4\rho_1} + \frac{\sqrt{-(16\rho_1\rho_3-5\rho_2^2)}}{4\rho_1} \mathrm{nc}\left[\frac{\sqrt{-(4\rho_1\rho_3-\rho_2^2)\rho_1}}{2\rho_1}\xi, \frac{\rho_2}{2\sqrt{(4\rho_1\rho_3-\rho_2^2)}}\right], \tag{2.10}$$

$$Q_{1,6}(\xi) = -\frac{\rho_2}{4\rho_1} + \frac{\sqrt{-(16\rho_1\rho_3-5\rho_2^2)}}{4\rho_1}\mathrm{nd}\left[\frac{\rho_2}{4\sqrt{-\rho_1}}\xi, \frac{2\sqrt{(4\rho_1\rho_3-\rho_2^2)}}{\rho_2}\right]. \tag{2.11}$$

Sub-Case 1.4. If $\rho_1(4\rho_1\rho_3 - \rho_2^2) > 0$, and $(4\rho_1\rho_3 - \rho_2^2)(16\rho_1\rho_3 - 5\rho_2^2) > 0$, then

$$Q_{1,7}(\xi) = -\frac{\rho_2}{4\rho_1} + \frac{(16\rho_1\rho_3-5\rho_2^2)}{4\rho_1} \mathrm{nc}\left[\frac{\sqrt{\rho_1(4\rho_1\rho_3-\rho_2^2)}}{2\rho_1}\xi, \frac{\sqrt{(4\rho_1\rho_3-\rho_2^2)(16\rho_1\rho_3-5\rho_2^2)}}{\rho_1}\right], \tag{2.12}$$

$$Q_{1,8}(\xi) = -\frac{\rho_2}{4\rho_1} + \frac{(16\rho_1\rho_3-5\rho_2^2)}{4\rho_1} \mathrm{nd}\left[\frac{\sqrt{\rho_1(16\rho_1\rho_3-5\rho_2^2)}}{4\rho_1}\xi, \frac{2\sqrt{(4\rho_1\rho_3-\rho_2^2)(16\rho_1\rho_3-5\rho_2^2)}}{\rho_2}\right]. \tag{2.13}$$

Sub-Case 1.5. If $\rho_1 > 0$, and $(16\rho_1\rho_3 - 5\rho_2^2) < 0$, then

$$Q_{1,9}(\xi) = -\frac{\rho_2}{4\rho_1} + \frac{\rho_2}{4\rho_1}\mathrm{ns}\left[\frac{\rho_2}{4\sqrt{\rho_1}}\xi, \frac{\sqrt{-(16\rho_1\rho_3-5\rho_2^2)}}{\rho_2}\right], \tag{2.14}$$

$$Q_{1,10}(\xi) = -\frac{\rho_2}{4\rho_1} + \frac{\sqrt{-(16\rho_1\rho_3-5\rho_2^2)}}{4\rho_1} \mathrm{ns}\left[\frac{\sqrt{-\rho_1(16\rho_1\rho_3-5\rho_2^2)}}{4\rho_1}\xi, \frac{\rho_2}{\sqrt{-(16\rho_1\rho_3-5\rho_2^2)}}\right], \tag{2.15}$$

$$Q_{1,11}(\xi) = -\frac{\rho_2}{4\rho_1} + \frac{\sqrt{-(16\rho_1\rho_3-5\rho_2^2)}}{4\rho_1}\mathrm{sn}\left[\frac{\rho_2}{4\sqrt{\rho_1}}\xi, \frac{\sqrt{-(16\rho_1\rho_3-5\rho_2^2)}}{\rho_2}\right], \tag{2.16}$$

$$Q_{1,12}(\xi) = -\frac{\rho_2}{4\rho_1} + \frac{\rho_2}{4\rho_1}\mathrm{sn}\left[\frac{\sqrt{-\rho_1(16\rho_1\rho_3-5\rho_2^2)}}{4\rho_1}\xi, \frac{\rho_2}{\sqrt{-(16\rho_1\rho_3-5\rho_2^2)}}\right]. \tag{2.17}$$

In this instance, the elliptic modulus is represented by the 2nd term of the Jacobi elliptic functions. Therefore, m is the modulus of the elliptic function in $nd[\eta, m]$.

Case 2. If $\rho_4 = \frac{\rho_2\left(4\rho_1\rho_3-\rho_2^2\right)}{8\rho_1^2}$, $\rho_5 = \frac{\left(4\rho_1\rho_3-\rho_2^2\right)^2}{64\rho_1^3}$, then we get the **trigonometric and hyperbolic solutions** as follows:

Sub-Case 2.1. If $\rho_1 > 0$, and $(8\rho_1\rho_3 - 3\rho_2^2) < 0$, then

$$Q_{2,1}(\xi) = -\frac{\rho_2}{4\rho_1} + \frac{\sqrt{-(8\rho_1\rho_3-3\rho_2^2)}}{4\rho_1}\tanh\left[\frac{\sqrt{-\rho_1(8\rho_1\rho_3-3\rho_2^2)}}{4\rho_1}\xi\right], \tag{2.18}$$

$$Q_{2,2}(\xi) = -\frac{\rho_2}{4\rho_1} + \frac{\sqrt{-(8\rho_1\rho_3-3\rho_2^2)}}{4\rho_1}\coth\left[\frac{\sqrt{-\rho_1(8\rho_1\rho_3-3\rho_2^2)}}{4\rho_1}\xi\right]. \tag{2.19}$$

Sub-Case 2.2. If $\rho_1 > 0$, and $(8\rho_1\rho_3 - 3\rho_2^2) > 0$, then

$$Q_{2,3}(\xi) = -\frac{\rho_2}{4\rho_1} + \frac{\sqrt{(8\rho_1\rho_3-3\rho_2^2)}}{4\rho_1}\tan\left[\frac{\sqrt{\rho_1(8\rho_1\rho_3-3\rho_2^2)}}{4\rho_1}\xi\right], \tag{2.20}$$

$$Q_{2,4}(\xi) = -\frac{\rho_2}{4\rho_1} + \frac{\sqrt{(8\rho_1\rho_3-3\rho_2^2)}}{4\rho_1}\cot\left[\frac{\sqrt{\rho_1(8\rho_1\rho_3-3\rho_2^2)}}{4\rho_1}\xi\right]. \tag{2.21}$$

Case 3. If $\rho_4 = \frac{\rho_2\left(4\rho_1\rho_3-\rho_2^2\right)}{8\rho_1^2}$, and $\rho_5 = \frac{\rho_2^2\left(16\rho_1\rho_3-5\rho_2^2\right)^2}{256\rho_1^3}$, then we obtain the **hyperbolic and trigonometric solutions** as follows:

Sub-Case 3.1. If $\rho_1 < 0$, and $(8\rho_1\rho_3 - 3\rho_2^2) < 0$, then

$$Q_{3,1}(\xi) = -\frac{\rho_2}{4\rho_1} + \frac{\sqrt{-2(8\rho_1\rho_3-3\rho_2^2)}}{4\rho_1}\mathrm{sech}\left[\frac{\sqrt{2\rho_1(8\rho_1\rho_3-3\rho_2^2)}}{4\rho_1}\xi\right]. \tag{2.22}$$

Sub-Case 3.2. If $\rho_1 > 0$, and $(8\rho_1\rho_3 - 3\rho_2^2) > 0$, then

$$Q_{3,2}(\xi) = -\frac{\rho_2}{4\rho_1} + \frac{\sqrt{2(8\rho_1\rho_3 - 3\rho_2^2)}}{4\rho_1}\operatorname{csch}\left[\frac{\sqrt{2\rho_1(8\rho_1\rho_3 - 3\rho_2^2)}}{4\rho_1}\xi\right]. \tag{2.23}$$

Sub-Case 3.3. If $\rho_1 > 0$, and $(8\rho_1\rho_3 - 3\rho_2^2) < 0$, then

$$Q_{3,3}(\xi) = -\frac{\rho_2}{4\rho_1} + \frac{\sqrt{-2(8\rho_1\rho_3 - 3\rho_2^2)}}{4\rho_1}\sec\left[\frac{\sqrt{-2\rho_1(8\rho_1\rho_3 - 3\rho_2^2)}}{4\rho_1}\xi\right], \tag{2.24}$$

$$Q_{3,4}(\xi) = -\frac{\rho_2}{4\rho_1} + \frac{\sqrt{-2(8\rho_1\rho_3 - 3\rho_2^2)}}{4\rho_1}\csc\left[\frac{\sqrt{-2\rho_1(8\rho_1\rho_3 - 3\rho_2^2)}}{4\rho_1}\xi\right]. \tag{2.25}$$

Case 4. If $\rho_2 = 0, \quad \rho_4 = 0, \quad \rho_5 = 0, \quad \rho_3 > 0$, then we achieve the **exponential solutions** as follows:

$$Q_{4,1}(\xi) = \frac{4\varsigma\rho_3}{4\varsigma^2\exp\left[\sqrt{\rho_3}\xi\right] - \rho_1\rho_3\exp\left[-\sqrt{\rho_3}\xi\right]}. \tag{2.26}$$

Sub-Case 4.1. If $\rho_1 = -\frac{4\varsigma^2}{\rho_3}$, Eq.(2.26) reduces to

$$Q_{4,2}(\xi) = \frac{\rho_3}{2\varsigma}sech\left[-\sqrt{\rho_3}\xi\right]. \tag{2.27}$$

Sub-Case 4.2. If $\rho_1 = \frac{4\varsigma^2}{\rho_3}$, Eq.(2.26) reduces to

$$Q_{4,3}(\xi) = \frac{\rho_3}{2\varsigma}csch\left[-\sqrt{\rho_3}\xi\right]. \tag{2.28}$$

Having outlined the mathematical model and the Kumar-Malik method, we now apply this technique to derive explicit analytical solutions of the proposed Boussinesq-type KdV equation. By classifying the solutions based on functional forms, we explore the rich soliton structures inherent in the model.

3. Analytical solutions via Kumar-Malik method

Thanks to transformation Eq. (2.2),

$$\Phi(x, y, z, t) = \Phi(\xi), \quad \xi = kx + ly + mz + nt, \tag{3.1}$$

where k, l, m, n are the wave speed constants, Eq. (1.4) transforms it into an ODE:

$$\gamma k^4\Phi'' + \left(k(dm + fn + \theta l) + k^2 + n^2\right)\Phi + \lambda k^2\Phi^2 = 0. \tag{3.2}$$

By using the balancing principle on Eq. (3.2), we obtain $N = 2$. Therefore, Eq. (2.4) becomes:

$$\Phi(\xi) = A_0 + A_1 Q(\xi) + A_2 Q(\xi)^2. \tag{3.3}$$

The following set of algebraic equations can be obtained by following the method's steps:

$$\begin{cases} Q(\xi)^4 : 6\gamma k^4 A_2\rho_1 + k^2\lambda {A_2}^2 = 0, \\ Q(\xi)^3 : 2\gamma k^4 A_1\rho_1 + 5\gamma k^4 A_2\rho_2 + 2k^2\lambda A_1 A_2 = 0, \\ Q(\xi)^2 : k^2\lambda {A_1}^2 + A_2 k^2 + A_2 n^2 + A_2 dkm + A_2 fkn + A_2 kl\theta \\ \quad +2k^2\lambda A_2 A_0 + 4k^4\gamma A_2\rho_3 + 3/2\, k^4\gamma A_1\rho_2 = 0, \\ Q(\xi)^1 : \gamma k^4 A_1\rho_3 + 3\gamma k^4 A_2\rho_4 + 2k^2\lambda A_0 A_1 + dkmA_1 + fknA_1 \\ \quad +kl\theta A_1 + k^2 A_1 + n^2 A_1 = 0, \\ Q(\xi)^0 : A_0 dkm + A_0 fkn + A_0 kl\theta + 1/2\, k^4\gamma A_1\rho_4 + 2k^4\gamma A_2\rho_5 \\ \quad +k^2\lambda {A_0}^2 + A_0 k^2 + A_0 n^2 = 0. \end{cases} \tag{3.4}$$

3.1. *Jacobi Elliptic function solutions ($\Phi_{1,1}(x, y, z, t)$ to $\Phi_{1,12}(x, y, z, t)$)*

When we solve the above algebraic system, we get

$$\theta = -\frac{k^4\sqrt{\gamma^2\left(256\rho_1^2\rho_3^2 - 144\rho_3\rho_2^2\rho_1 + 21\rho_2^4\right)} + 4dkm\rho_1 + 4fkn\rho_1 + 4k^2\rho_1 + 4n^2\rho_1}{4l\rho_1 k}, \tag{3.5}$$

$$A_0 = \frac{\left(-16\gamma\rho_1\rho_3 + 3\gamma\rho_2^2 + \sqrt{\gamma^2\left(256\rho_1^2\rho_3^2 - 144\rho_3\rho_2^2\rho_1 + 21\rho_2^4\right)}\right)k^2}{8\rho_1\lambda},$$

$$A_1 = -\frac{3\gamma k^2\rho_2}{\lambda}, \quad A_2 = -\frac{6\rho_1\gamma k^2}{\lambda}. \tag{3.6}$$

Case 1. If Eq. (3.6) is inserted into Eq. (3.3) to provide the comprehensive solution to Eq. (1.4) for $\rho_4 = \frac{\rho_2\left(4\rho_1\rho_3 - \rho_2^2\right)}{8\rho_1^2}$, $\rho_5 = 0$:

Sub-Case 1.1. If $\rho_1 < 0$, and $4\rho_1\rho_3 - \rho_2^2 > 0$, then we get

$$\Phi_{1,1}(x, y, z, t) = \frac{1}{8\rho_1\lambda}\left(\gamma k^2\left(\Phi_{1,1} = \frac{1}{8\rho_1\lambda}\left(\gamma k^2\left(\begin{array}{l} -3\operatorname{cn}\left[\frac{\sqrt{-\rho_1\left(4\rho_1\rho_3 - \rho_2^2\right)}}{2\rho_1}(kx + ly + mz + nt), \frac{\rho_2}{2\sqrt{4\rho_1\rho_3 - \rho_2^2}}\right]^2 \rho_2^2 \\ -16\rho_1\rho_3 + 6\rho_2^2 + \sqrt{256\rho_1^2\rho_3^2 - 144\rho_3\rho_2^2\rho_1 + 21\rho_2^4} \end{array}\right)\right)\right)\right), \tag{3.7}$$

$$\Phi_{1,2}(x, y, z, t) = \frac{1}{8\rho_1\lambda}\left(\gamma k^2\left(\begin{array}{l} -3\operatorname{dn}\left[\frac{\rho_2}{4\sqrt{-\rho_1}}(kx + ly + mz + nt), \frac{2\sqrt{4\rho_1\rho_3 - \rho_2^2}}{\rho_2}\right]^2 \rho_2^2 \\ -16\rho_1\rho_3 + 6\rho_2^2 + \sqrt{256\rho_1^2\rho_3^2 - 144\rho_3\rho_2^2\rho_1 + 21\rho_2^4} \end{array}\right)\right). \tag{3.8}$$

Sub-Case 1.2. If $\rho_1 < 0$, $4\rho_1\rho_3 - \rho_2^2 < 0$, and $(16\rho_1\rho_3 - 5\rho_2^2) < 0$, then we get

$$\Phi_{1,3}(x, y, z, t) = \frac{1}{8\rho_1\lambda}\left(\gamma k^2\left(\begin{array}{l} 48\operatorname{cn}\left[\frac{\sqrt{\rho_1\left(4\rho_1\rho_3 - \rho_2^2\right)}}{2\rho_1}(kx + ly + mz + nt), \frac{\sqrt{(4\rho_1\rho_3 - \rho_2^2)(16\rho_1\rho_3 - 5\rho_2^2)}}{2\left(4\rho_1\rho_3 - \rho_2^2\right)}\right]^2 \rho_1\rho_3 \\ -15\operatorname{cn}\left[\frac{\sqrt{\rho_1\left(4\rho_1\rho_3 - \rho_2^2\right)}}{2\rho_1}(kx + ly + mz + nt), \frac{\sqrt{(4\rho_1\rho_3 - \rho_2^2)(16\rho_1\rho_3 - 5\rho_2^2)}}{2\left(4\rho_1\rho_3 - \rho_2^2\right)}\right]^2 \rho_2^2 \\ -16\rho_1\rho_3 + 6\rho_2^2 + \sqrt{256\rho_1^2\rho_3^2 - 144\rho_3\rho_2^2\rho_1 + 21\rho_2^4} \end{array}\right)\right), \tag{3.9}$$

$$\Phi_{1,4}(x, y, z, t) = \frac{1}{8\rho_1\lambda}\left(\gamma k^2\left(\begin{array}{l} 48\operatorname{dn}\left[\frac{\sqrt{\rho_1\left(16\rho_1\rho_3 - 5\rho_2^2\right)}}{4\rho_1}(kx + ly + mz + nt), \frac{2\sqrt{(4\rho_1\rho_3 - \rho_2^2)(16\rho_1\rho_3 - 5\rho_2^2)}}{16\rho_1\rho_3 - 5\rho_2^2}\right]^2 \rho_1\rho_3 \\ -15\operatorname{dn}\left[\frac{\sqrt{\rho_1\left(16\rho_1\rho_3 - \rho_2^2\right)}}{4\rho_1}(kx + ly + mz + nt), \frac{2\sqrt{(4\rho_1\rho_3 - \rho_2^2)(16\rho_1\rho_3 - 5\rho_2^2)}}{16\rho_1\rho_3 - 5\rho_2^2}\right]^2 \rho_2^2 \\ -16\rho_1\rho_3 + 6\rho_2^2 + \sqrt{256\rho_1^2\rho_3^2 - 144\rho_3\rho_2^2\rho_1 + 21\rho_2^4} \end{array}\right)\right). \tag{3.10}$$

Sub-Case 1.3. If $\rho_1 < 0$, $4\rho_1\rho_3 - \rho_2^2 > 0$, and $(16\rho_1\rho_3 - 5\rho_2^2) < 0$, then we get

$$\Phi_{1,5}(x, y, z, t) = \frac{1}{8\rho_1\lambda}\left(\gamma k^2\left(\begin{array}{l} 48\operatorname{nd}\left[\frac{\sqrt{-\rho_1\left(4\rho_1\rho_3 - \rho_2^2\right)}}{2\rho_1}(kx + ly + mz + nt), \frac{\rho_2}{2\sqrt{4\rho_1\rho_3 - \rho_2^2}}\right]^2 \rho_1\rho_3 \\ -15\operatorname{nd}\left[\frac{\sqrt{-\rho_1\left(4\rho_1\rho_3 - \rho_2^2\right)}}{2\rho_1}(kx + ly + mz + nt), \frac{\rho_2}{2\sqrt{4\rho_1\rho_3 - \rho_2^2}}\right]^2 \rho_2^2 \\ -16\rho_1\rho_3 + 6\rho_2^2 + \sqrt{256\rho_1^2\rho_3^2 - 144\rho_3\rho_2^2\rho_1 + 21\rho_2^4} \end{array}\right)\right), \tag{3.11}$$

$$\Phi_{1,6}(x, y, z, t) =$$

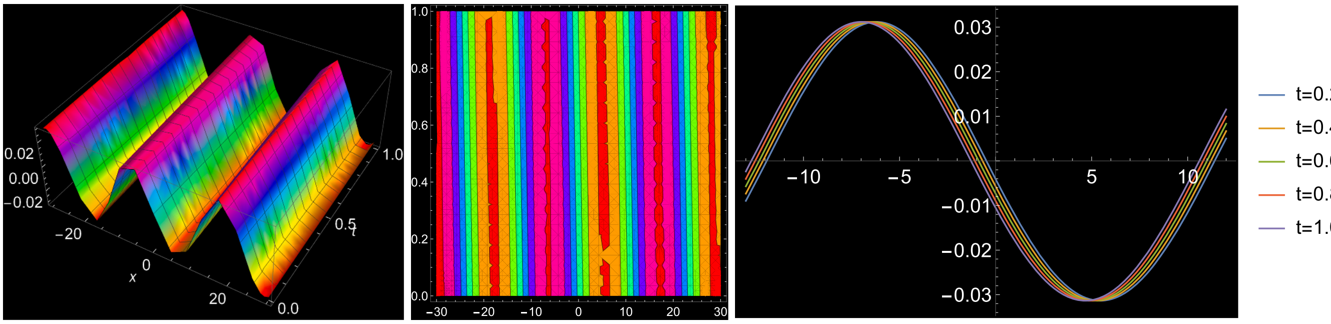

Fig. 1. (a) The 3D soliton, (b) contour and (c) 2D plot of $\Phi_{1,1}(x,y,z,t)$ appearing in Eq. (3.7) for the values $\rho_1=-3$, $\rho_2=1$, $\rho_3=-2$, $k=0.1$, $l=0.5$, $m=0.1$, $n=0.1$, $\gamma=5$, $y=1$, $z=1$, $\lambda=0.1$.

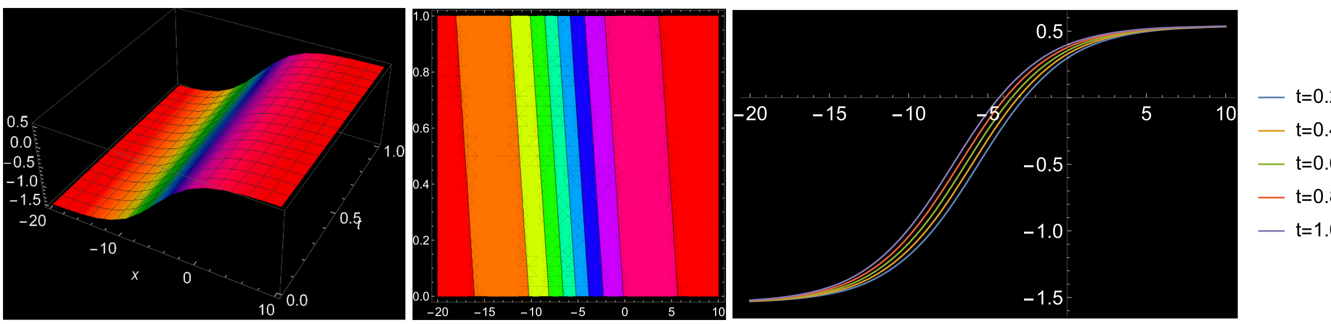

Fig. 2. (a) The 3D soliton, (b) contour and (c) 2D plot of $\Phi_{2,1}(x,y,z,t)$ appearing in Eq. (3.19) for the values $\rho_1=3$, $\rho_2=6$, $\rho_3=-2$, $k=0.1$, $l=0.5$, $m=0.1$, $n=0.2$, $y=1$, $z=0.2$, $\lambda=1$.

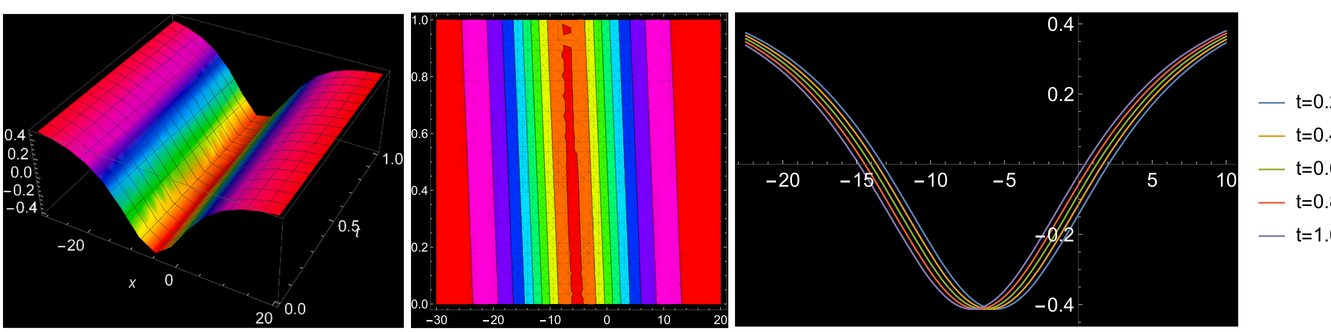

Fig. 3. (a) The 3D soliton, (b) contour and (c) 2D plot of $\Phi_{3,1}(x,y,z,t)$ appearing in Eq. (3.23) for the values $\rho_1=-3$, $\rho_2=6$, $\rho_3=-2$, $k=0.1$, $l=0.5$, $m=0.1$, $n=0.2$, $y=1$, $z=0.2$, $\lambda=1$.

$$\frac{1}{8\rho_1\lambda}\left(\gamma k^2\left(\begin{array}{l}48\mathrm{nd}\left[\frac{\rho_2}{4\sqrt{-\rho_1}}(kx+ly+mz+nt),\frac{2\sqrt{4\rho_1\rho_3-\rho_2^2}}{\rho_2}\right]^2\rho_1\rho_3\\ -15\mathrm{nd}\left[\frac{\rho_2}{4\sqrt{-\rho_1}}(kx+ly+mz+nt),\frac{2\sqrt{4\rho_1\rho_3-\rho_2^2}}{\rho_2}\right]^2\rho_2^2\\ -16\rho_1\rho_3+6\rho_2^2+\sqrt{256\rho_1^2\rho_3^2-144\rho_3\rho_2^2\rho_1+21\rho_2^4}\end{array}\right)\right). \tag{3.12}$$

Sub-Case 1.4. If $\rho_1(4\rho_1\rho_3-\rho_2^2)>0$, and $(4\rho_1\rho_3-\rho_2^2)(16\rho_1\rho_3-5\rho_2^2)>0$, then we get

$$\Phi_{1,7}(x,y,z,t)=$$
$$\frac{1}{8\rho_1\lambda}\left(\gamma k^2\left(\begin{array}{l}-3\mathrm{nd}\left[\frac{\sqrt{\rho_1\left(4\rho_1\rho_3-\rho_2^2\right)}}{2\rho_1}(kx+ly+mz+nt),\frac{(4\rho_1\rho_3-\rho_2^2)(16\rho_1\rho_3-5\rho_2^2)}{2\sqrt{4\rho_1\rho_3-\rho_2^2}}\right]^2\rho_2^2\\ -16\rho_1\rho_3+6\rho_2^2+\sqrt{256\rho_1^2\rho_3^2-144\rho_3\rho_2^2\rho_1+21\rho_2^4}\end{array}\right)\right), \tag{3.13}$$

$$\Phi_{1,8}(x,y,z,t)=\frac{1}{8\rho_1\lambda}$$
$$\left(\gamma k^2\left(\begin{array}{l}-3\mathrm{nd}\left[\frac{\sqrt{\rho_1\left(16\rho_1\rho_3-5\rho_2^2\right)}}{4\rho_1}(kx+ly+mz+nt),\frac{2\sqrt{(4\rho_1\rho_3-\rho_2^2)(16\rho_1\rho_3-5\rho_2^2)}}{16\rho_1\rho_3-5\rho_2^2}\right]^2\rho_2^2\\ -16\rho_1\rho_3+6\rho_2^2+\sqrt{256\rho_1^2\rho_3^2-144\rho_3\rho_2^2\rho_1+21\rho_2^4}\end{array}\right)\right). \tag{3.14}$$

Sub-Case 1.5. If $\rho_1>0$, and $(16\rho_1\rho_3-5\rho_2^2)<0$, then we get

$$\Phi_{1,9}(x,y,z,t)=\frac{1}{8\rho_1\lambda}$$
$$\left(\gamma k^2\left(\begin{array}{l}-3\mathrm{ns}\left[\frac{\rho_2}{4\sqrt{\rho_1}}(kx+ly+mz+nt),\frac{\sqrt{-16\rho_1\rho_3+5\rho_2^2}}{\rho_2}\right]^2\rho_2^2\\ -16\rho_1\rho_3+6\rho_2^2+\sqrt{256\rho_1^2\rho_3^2-144\rho_3\rho_2^2\rho_1+21\rho_2^4}\end{array}\right)\right), \tag{3.15}$$

$$\Phi_{1,10}(x,y,z,t)=\frac{1}{8\rho_1\lambda}$$

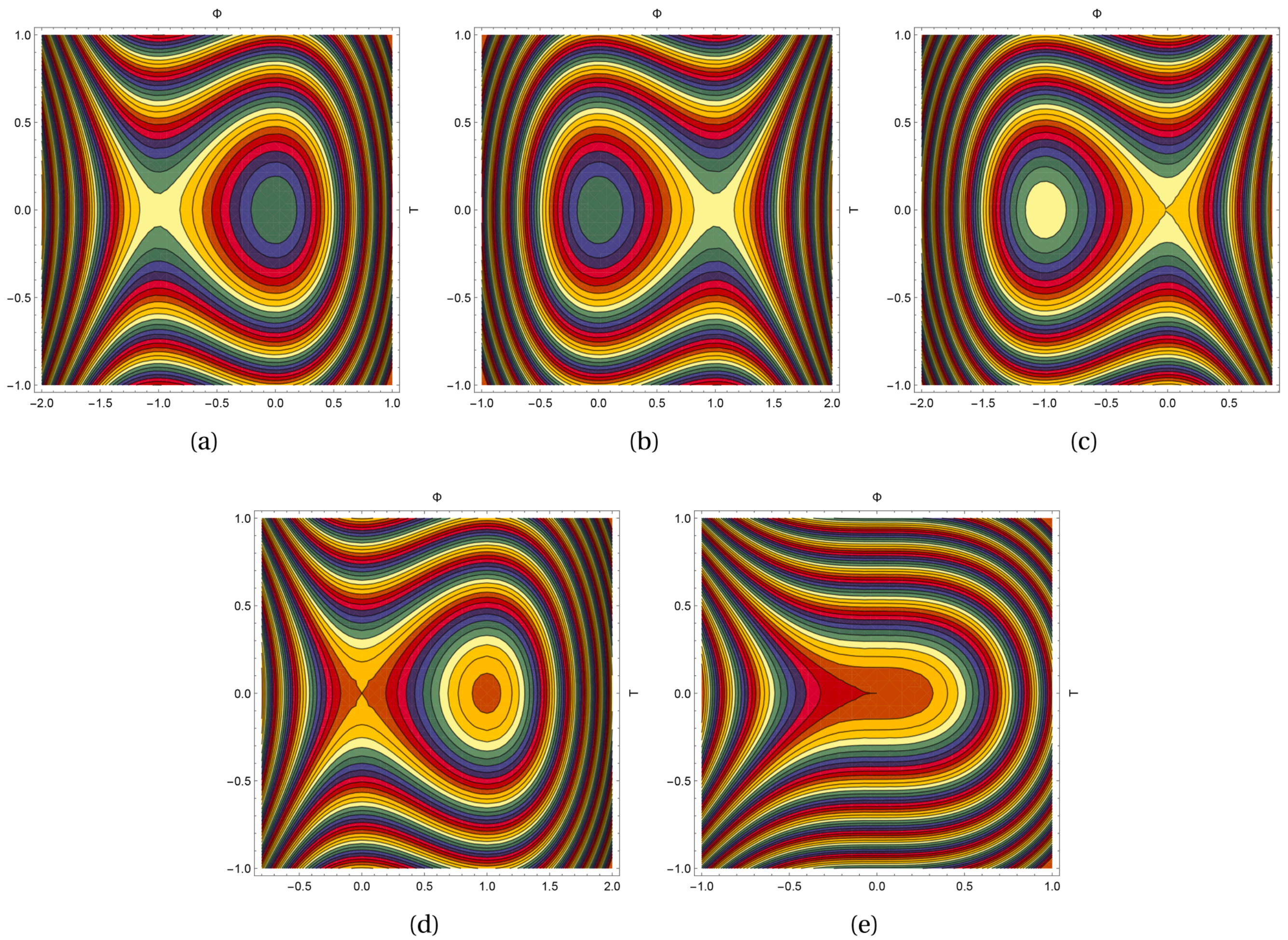

Fig. 4. Phase-portraits of the reduced system (5.1) using the values $k=1$, $d=0$, $m=0.15$, $f=0.1$, $n=0.2$, $l=0.5$, $\theta=0.3$, $\gamma=1.21$, $\lambda=1.21$, and **a.)** $w_1=1$, $w_2=1$, **b.)** $w_1=1$, $w_2=-1$, **c.)** $w_1=-1$, $w_2=-1$, **d.)** $w_1=-1$, $w_2=1$, **e.)** $w_1=0$, $w_2=1$.

$$\left(\gamma k^2\left(\begin{array}{l} 48\,\mathrm{ns}\left[\frac{\sqrt{-\rho_1\left(16\rho_1\rho_3-5\rho_2^2\right)}}{4\rho_1}(kx+ly+mz+nt),\ \frac{\rho_2}{\sqrt{-16\rho_1\rho_3+5\rho_2^2}}\right]^2\rho_1\rho_3 \\ -15\,\mathrm{ns}\left[\frac{\sqrt{-\rho_1\left(16\rho_1\rho_3-\rho_2^2\right)}}{4\rho_1}(kx+ly+mz+nt),\ \frac{\rho_2}{\sqrt{-16\rho_1\rho_3+5\rho_2^2}}\right]^2\rho_2^2 \\ -16\rho_1\rho_3+6\rho_2^2+\sqrt{256\rho_1^2\rho_3^2-144\rho_3\rho_2^2\rho_1+21\rho_2^4} \end{array}\right)\right), \tag{3.16}$$

$$\Phi_{1,11}(x,y,z,t)=\frac{1}{8\rho_1\lambda}$$
$$\left(\gamma k^2\left(\begin{array}{l} 48\,\mathrm{sn}\left[\frac{\rho_2}{4\sqrt{\rho_1}}(kx+ly+mz+nt),\ \frac{\sqrt{-16\rho_1\rho_3+5\rho_2^2}}{\rho_2}\right]^2\rho_1\rho_3 \\ -15\,\mathrm{sn}\left[\frac{\rho_2}{4\sqrt{\rho_1}}(kx+ly+mz+nt),\ \frac{\sqrt{-16\rho_1\rho_3+5\rho_2^2}}{\rho_2}\right]^2\rho_2^2 \\ -16\rho_1\rho_3+6\rho_2^2+\sqrt{256\rho_1^2\rho_3^2-144\rho_3\rho_2^2\rho_1+21\rho_2^4} \end{array}\right)\right), \tag{3.17}$$

$$\Phi_{1,12}(x,y,z,t)=\frac{1}{8\rho_1\lambda}$$
$$\left(\gamma k^2\left(\begin{array}{l} -3\,\mathrm{sn}\left[\frac{\sqrt{-\rho_1\left(16\rho_1\rho_3-5\rho_2^2\right)}}{4\rho_1}(kx+ly+mz+nt),\ \frac{\rho_2}{\sqrt{-16\rho_1\rho_3+5\rho_2^2}}\right]^2\rho_2^2 \\ -16\rho_1\rho_3+6\rho_2^2+\sqrt{256\rho_1^2\rho_3^2-144\rho_3\rho_2^2\rho_1+21\rho_2^4} \end{array}\right)\right). \tag{3.18}$$

3.2. Trigonometric and hyperbolic function solutions ($\Phi_{2,1}(x,y,z,t)$ to $\Phi_{2,4}(x,y,z,t)$ and $\Phi_{3,1}(x,y,z,t)$ to $\Phi_{3,4}(x,y,z,t)$)

Case 2. For $\rho_4=\frac{\rho_2\left(4\rho_1\rho_3-\rho_2^2\right)}{8\rho_1^2}$, $\rho_5=\frac{\left(4\rho_1\rho_3-\rho_2^2\right)^2}{64\rho_1^3}$, the solutions are as follows:

Sub-Case 2.1. If $\rho_1>0$, and $(8\rho_1\rho_3-3\rho_2^2)<0$, then we get

$$\Phi_{2,1}(x,y,z,t)=\frac{3\gamma k^2}{8\rho_1\lambda}\left(\tanh\left[\frac{\sqrt{-\rho_1\left(8\rho_1\rho_3-3\rho_2^2\right)}}{4\rho_1}(kx+ly+mz+nt)\right]-1\right)$$
$$\times\left(\tanh\left[\frac{\sqrt{-\rho_1\left(8\rho_1\rho_3-3\rho_2^2\right)}}{4\rho_1}(kx+ly+mz+nt)\right]+1\right)\times\left(8\rho_1\rho_3-3\rho_2^2\right), \tag{3.19}$$

$$\Phi_{2,2}(x,y,z,t)=\frac{3\gamma k^2}{8\rho_1\lambda}\left(\coth\left[\frac{\sqrt{-\rho_1\left(8\rho_1\rho_3-3\rho_2^2\right)}}{4\rho_1}(kx+ly+mz+nt)\right]-1\right)$$
$$\times\left(\coth\left[\frac{\sqrt{-\rho_1\left(8\rho_1\rho_3-3\rho_2^2\right)}}{4\rho_1}(kx+ly+mz+nt)\right]+1\right)\times\left(8\rho_1\rho_3-3\rho_2^2\right). \tag{3.20}$$

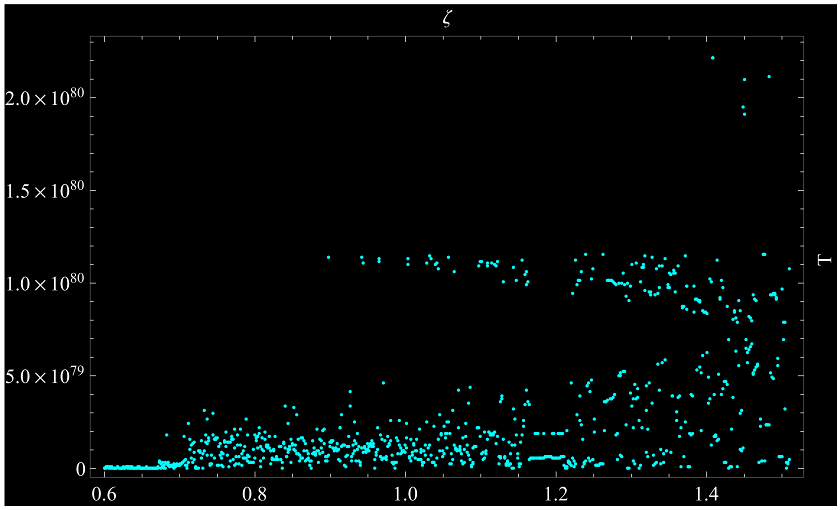

Fig. 5. Bifurcation diagram of the perturbed system (6.1) using the values $k = 1$, $d = 0$, $m = 0.15$, $f = 0.1$, $n = 1.196$, $l = 0.5$, $\theta = 0.4$, $\gamma = -1.1$, $\lambda = -1.65$ with the initial condition $(\Phi(0), T(0)) = (0.29, 0.13)$.

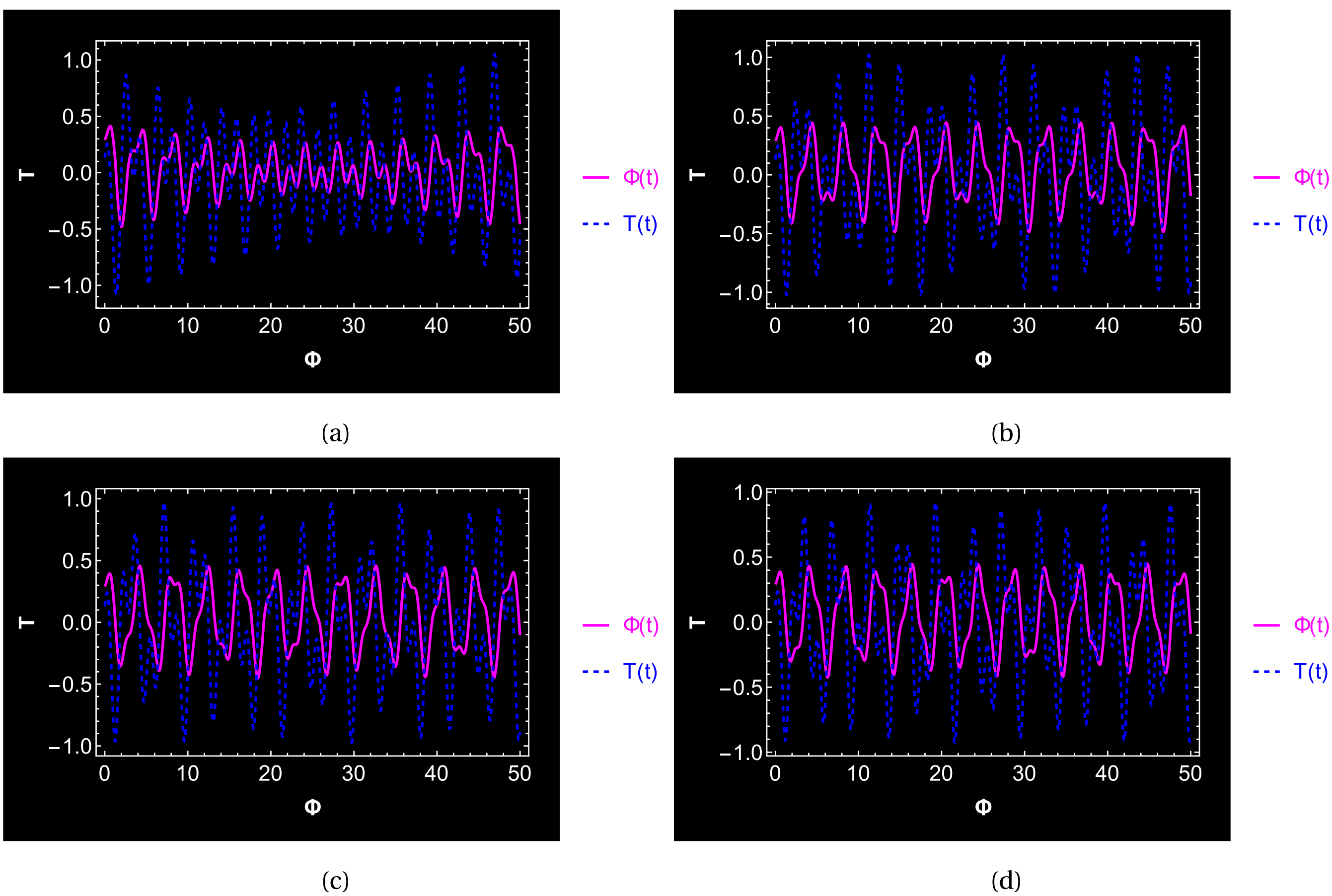

Fig. 6. Sensitivity analysis of the perturbed system (6.1) using the values $k = 1$, $d = 0$, $m = 0.15$, $f = 0.1$, $n = 1.196$, $l = 0.5$, $\theta = 0.4$, $\gamma = -1.1$, $\lambda = -1.65$, $f_0 = 1.25$, and **a.)** $\delta = 3.25$, **b.)** $\delta = 3.50$, **c.)** $\delta = 3.75$, **d.)** $\delta = 4.00$ with the initial condition $(\Phi(0), T(0)) = (0.29, 0.13)$.

Sub-Case 2.2. If $\rho_1 > 0$, and $(8\rho_1\rho_3 - 3\rho_2^2) > 0$, then we get

$$\Phi_{2,3}(x, y, z, t) = -\frac{3\gamma k^2}{8\rho_1\lambda}\left(\tan\left[\frac{\sqrt{\rho_1\left(8\rho_1\rho_3-3\rho_2^2\right)}}{4\rho_1}(kx + ly + mz + nt)\right]^2 + 1\right) \times \left(8\rho_1\rho_3 - 3\rho_2^2\right), \tag{3.21}$$

$$\Phi_{2,4}(x, y, z, t) = -\frac{3\gamma k^2}{8\rho_1\lambda}\left(\cot\left[\frac{\sqrt{\rho_1\left(8\rho_1\rho_3-3\rho_2^2\right)}}{4\rho_1}(kx + ly + mz + nt)\right]^2 + 1\right) \times \left(8\rho_1\rho_3 - 3\rho_2^2\right). \tag{3.22}$$

Case 3. For $\rho_4 = \frac{\rho_2\left(4\rho_1\rho_3-\rho_2^2\right)}{8\rho_1^2}$, $\quad \rho_5 = \frac{\left(4\rho_1\rho_3-\rho_2^2\right)^2}{64\rho_1^3}$, the solutions are as follows:

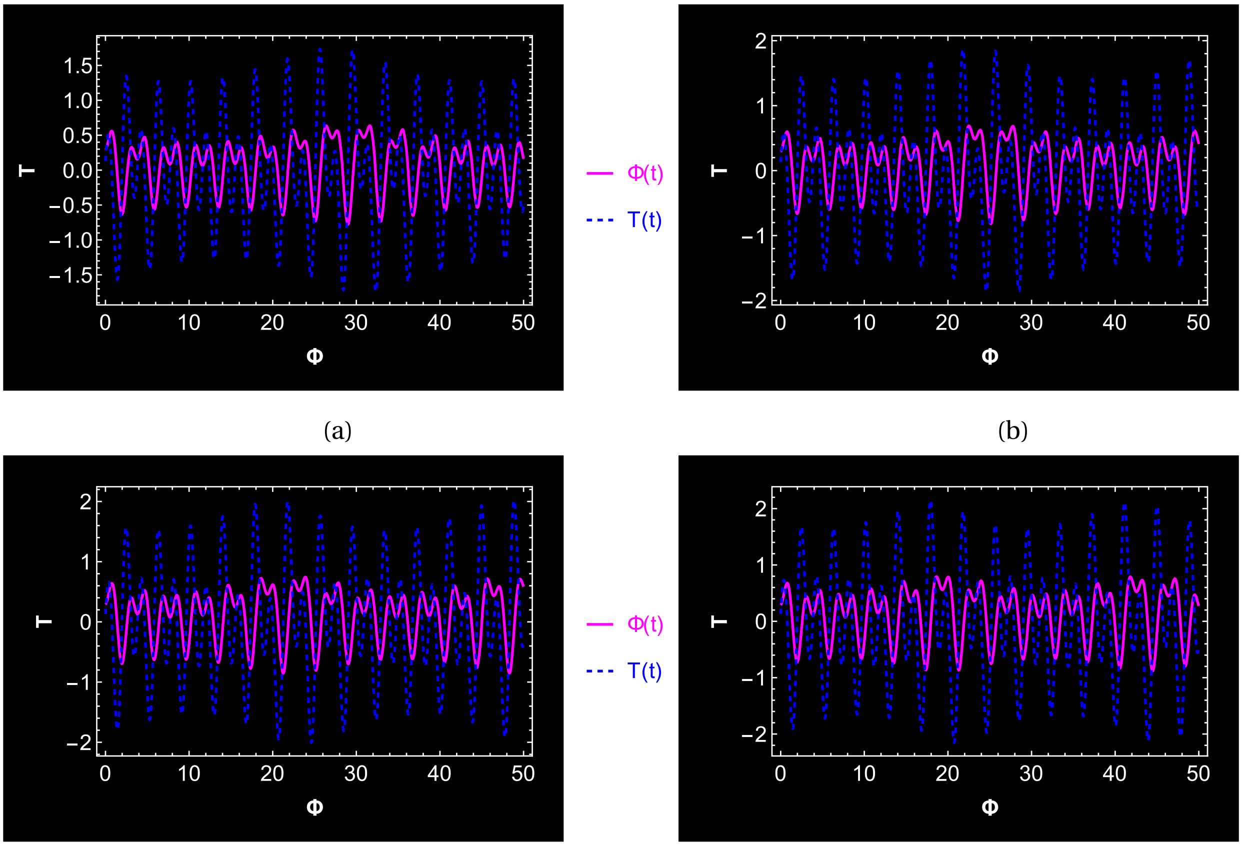

(a) (b)

(c) (d)

Fig. 7. Sensitivity analysis of the perturbed system (6.1) using the values $k=1$, $d=0$, $m=0.15$, $f=0.1$, $n=1.196$, $l=0.5$, $\theta=0.4$, $\gamma=-1.1$, $\lambda=-1.65$, $\delta=3.25$, and **a.)** $f_0=2.25$, **b.)** $f_0=2.50$, **c.)** $f_0=2.75$, **d.)** $f_0=3.00$ with the initial condition $(\Phi(0),T(0))=(0.29,0.13)$.

Sub-Case 3.1. If $\rho_1<0$, and $(8\rho_1\rho_3-3\rho_2^2)<0$, then we yield

$$\Phi_{3,1}(x,y,z,t)=\frac{3\gamma k^2}{4\rho_1\lambda}\left(\operatorname{sech}\left[\frac{\sqrt{2}\sqrt{\rho_1\left(8\rho_1\rho_3-3\rho_2^2\right)}}{4\rho_1}(kx+ly+mz+nt)\right]^2-2\right)\times\left(8\rho_1\rho_3-3\rho_2^2\right). \tag{3.23}$$

Sub-Case 3.2. If $\rho_1>0$, and $(8\rho_1\rho_3-3\rho_2^2)>0$, then we find

$$\Phi_{3,2}(x,y,z,t)=-\frac{3\gamma k^2}{4\rho_1\lambda}\left(\operatorname{csch}\left[\frac{\sqrt{2}\sqrt{\rho_1\left(8\rho_1\rho_3-3\rho_2^2\right)}}{4\rho_1}(kx+ly+mz+nt)\right]^2+2\right)\times\left(8\rho_1\rho_3-3\rho_2^2\right). \tag{3.24}$$

Sub-Case 3.3. If $\rho_1>0$, and $(8\rho_1\rho_3-3\rho_2^2)<0$, then we discover

$$\Phi_{3,3}(x,y,z,t)=\frac{3\gamma k^2}{4\rho_1\lambda}\left(\sec\left[\frac{\sqrt{-2\rho_1\left(8\rho_1\rho_3-3\rho_2^2\right)}}{4\rho_1}(kx+ly+mz+nt)\right]^2-2\right)\times\left(8\rho_1\rho_3-3\rho_2^2\right), \tag{3.25}$$

$$\Phi_{3,4}(x,y,z,t)=\frac{3\gamma k^2}{4\rho_1\lambda}\left(\csc\left[\frac{\sqrt{-2\rho_1\left(8\rho_1\rho_3-3\rho_2^2\right)}}{4\rho_1}(kx+ly+mz+nt)\right]^2-2\right)\times\left(8\rho_1\rho_3-3\rho_2^2\right). \tag{3.26}$$

3.3. Exponential function and trigonometric solutions ($\Phi_{4,1}(x,y,z,t)$ to $\Phi_{4,3}(x,y,z,t)$)

Case 4. For $\rho_2=\rho_4=\rho_5=0$, and $\rho_3>0$, then the solutions are as follows:

$$\Phi_{4,1}(x,y,z,t)=-\frac{\left\{4\gamma k^2\rho_3\left(\begin{array}{l}16\exp\left(\sqrt{\rho_3}(kx+ly+mz+nt)\right)^2\sigma^4-8\exp\left(\sqrt{\rho_3}(kx+ly+mz+nt)\right)\\ \times\exp\left(-\sqrt{\rho_3}(kx+ly+mz+nt)\right)\sigma^2\rho_1\rho_3\\ +\exp\left(-\sqrt{\rho_3}(kx+ly+mz+nt)\right)^2\rho_1^2\rho_3^2+24\sigma^2\rho_3\rho_1\end{array}\right)\right\}}{\lambda\left(4\sigma^2\exp\left(\sqrt{\rho_3}(kx+ly+mz+nt)\right)-\rho_1\rho_3\exp\left(-\sqrt{\rho_3}(kx+ly+mz+nt)\right)\right)^2}. \tag{3.27}$$

Sub-Case 4.1. If $\rho_1=-\frac{4\varsigma^2}{\rho_3}$, then we obtain

$$\Phi_{4,2}(x,y,z,t)=-\frac{\gamma k^2\rho_3}{2\lambda\sigma^2}\left(3\rho_1\rho_3\operatorname{sech}\left[\sqrt{\rho_3}(kx+ly+mz+nt)\right]^2+8\sigma^2\right). \tag{3.28}$$

Sub-Case 4.2. If $\rho_1=-\frac{4\varsigma^2}{\rho_3}$, then we reach

$$\Phi_{4,3}(x,y,z,t)=-\frac{\gamma k^2\rho_3}{2\lambda\sigma^2}\left(3\rho_1\rho_3\operatorname{csch}\left[\sqrt{\rho_3}(kx+ly+mz+nt)\right]^2+8\sigma^2\right). \tag{3.29}$$

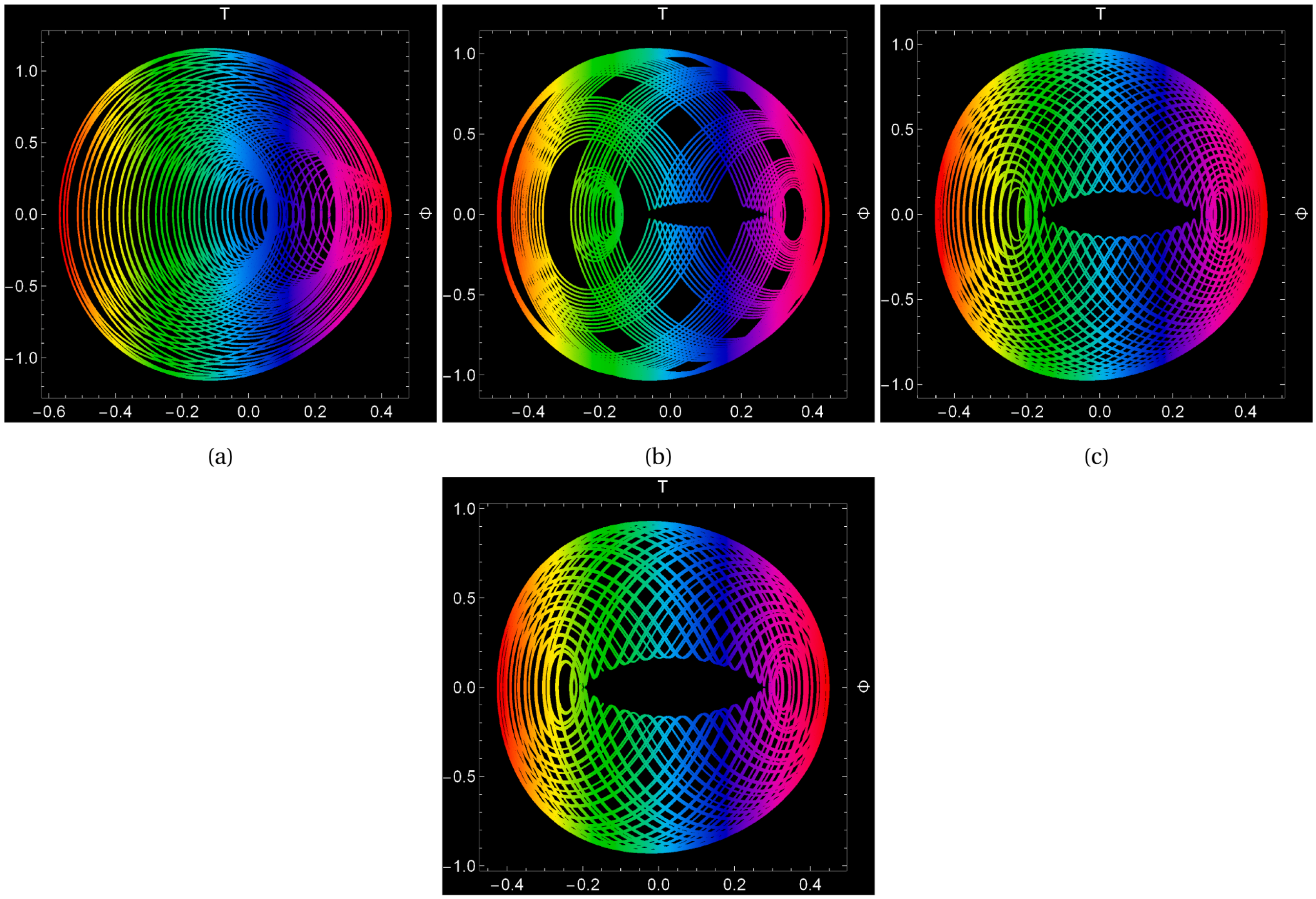

(a) (b) (c) (d)

Fig. 8. 2D chaotic analysis of the perturbed system (6.1) using the values $k = 1$, $d = 0$, $m = 0.15$, $f = 0.1$, $n = 1.196$, $l = 0.5$, $\theta = 0.4$, $\gamma = -1.1$, $\lambda = -1.65$, $f_0 = 1.25$, and **a.)** $\delta = 3.25$, **b.)** $\delta = 3.50$, **c.)** $\delta = 3.75$, **d.)** $\delta = 4.00$ with the initial condition $(\Phi(0), T(0)) = (0.29, 0.13)$.

The trigonometric and Jacobi-elliptic solutions derived above represent periodic waveforms of the extended Boussinesq-type KdV equation, corresponding to oscillatory soliton structures that maintain their periodicity due to the balance between nonlinearity and dispersion.

While the exact analytical solutions derived above yield mathematical insight, their physical and qualitative characteristics are best appreciated graphically. In this section, we graph representative solutions to ascertain their shape, stability, and evolution in time.

4. Visualization and interpretation of soliton structures

To observe the shape and dynamics of the analytical solutions derived, graphical plots are given for some cases concerning the solutions $\Phi_{1,1}(x, y, z, t)$, $\Phi_{2,1}(x, y, z, t)$, and $\Phi_{3,1}(x, y, z, t)$. The 3D soliton profile, contour plot, and 2D projection on a temporal slice in each plot reveal the wave structures' evolution and dynamics entirely.

4.1. Soliton profile of $\Phi_{1,1}(x, y, z, t)$

Fig. 1 illustrates the solution $\Phi_{1,1}(x, y, z, t)$ to Eq.(3.7) as a localized soliton profile. The one-peak soliton is preserved in form in the 3D plot as time progresses, which is evidence of its stability. The symmetric, bell-like form around the origin is clearly seen in the contour plot, and the smooth propagation without distortion in the 2D cross-sections for different values of time is exhibited, which confirms the stability of the soliton at the selected values of parameters.

The persistence of a single, symmetric crest with nearly invariant peak height indicates a near-stationary balance between nonlinear steepening and dispersive spreading. In the present parameter set, the dispersive contribution (scaled by γ and k) counteracts the quadratic and mixed-derivative nonlinearities (λ, θ), yielding a localized, bell-shaped pulse without oscillatory radiation. The concentric, evenly spaced contour bands corroborate weak transverse leakage, consistent with small l and m, and explain the negligible broadening in the temporal slices.

4.2. Soliton profile of $\Phi_{2,1}(x, y, z, t)$

Fig. 2 exhibits the solution $\Phi_{2,1}(x, y, z, t)$ of Eq. (3.19). It is a more intense and greater amplitude oscillation than the soliton of Fig. 1. A higher, more peaked profile is generated by the 3D plot, showing greater nonlinear effects for the same parameters. The contour plot also displays a tighter structure, and the time-evolution in the 2D plot exhibits breathing behavior, for which the amplitude dynamically changes with time, showing a likely modulation in the soliton profile.

Relative to Fig. 1, the higher peak and narrower footprint indicate stronger effective nonlinearity. The mild amplitude modulation (breathing) visible in the temporal slices suggests a near-resonant interplay between the dispersive term (controlled by γk^4 in the reduction) and the quadratic nonlinearity (scaled by λ). Tighter contour spacing around the crest reflects steeper flanks, while the phase-locked peak position implies a nearly constant effective velocity set by (k, n) in the traveling frame.

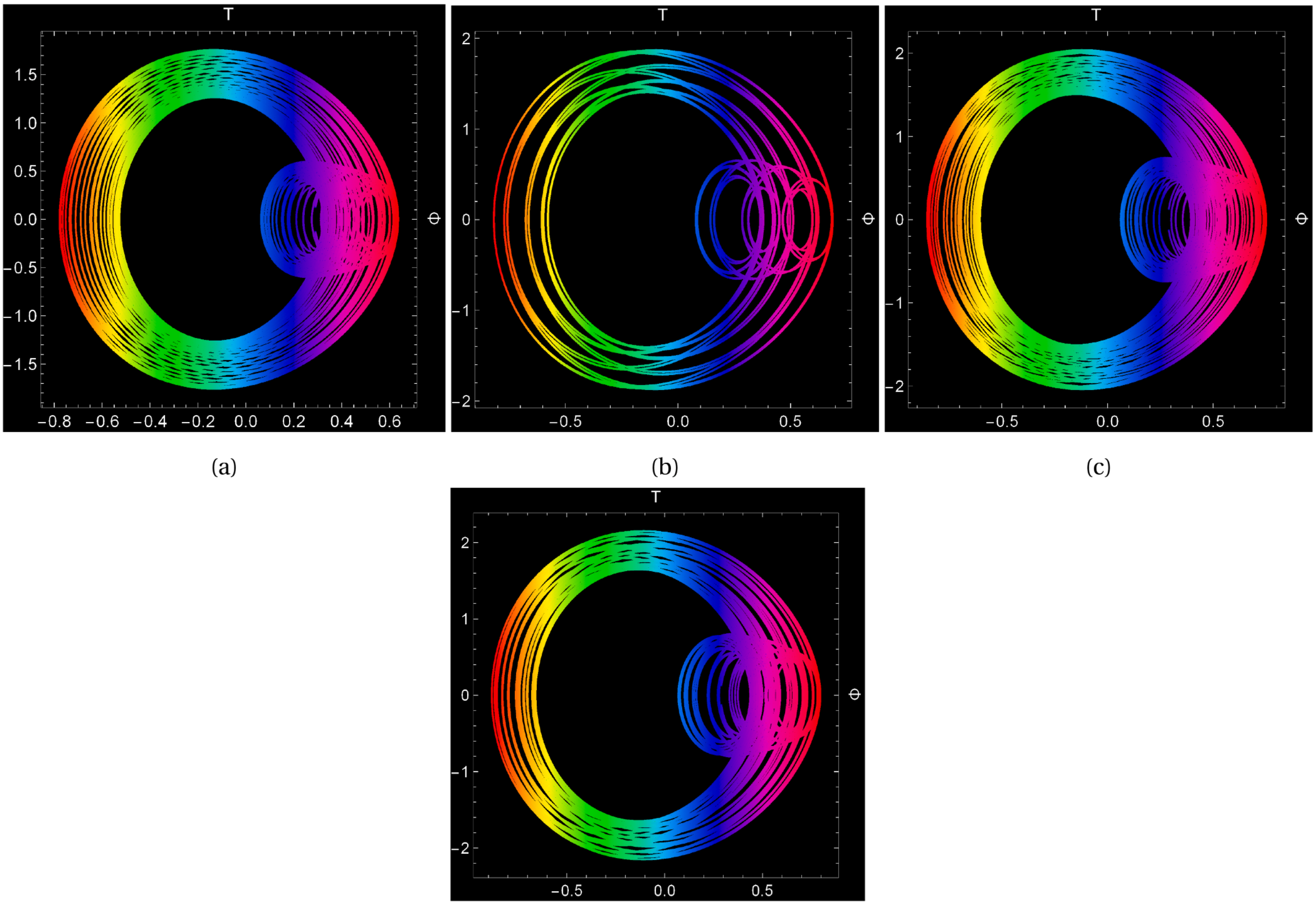

(a) (b) (c) (d)

Fig. 9. 2D chaotic analysis of the perturbed system (6.1) using the values $k = 1$, $d = 0$, $m = 0.15$, $f = 0.1$, $n = 1.196$, $l = 0.5$, $\theta = 0.4$, $\gamma = -1.1$, $\lambda = -1.65$, $\delta = 3.25$, and **a.)** $f_0 = 2.25$, **b.)** $f_0 = 2.50$, **c.)** $f_0 = 2.75$, **d.)** $f_0 = 3.00$ with the initial condition $(\Phi(0), T(0)) = (0.29, 0.13)$.

4.3. Soliton profile of $\Phi_{3,1}(x, y, z, t)$

Fig. 3 is the solution $\Phi_{3,1}(x, y, z, t)$ of Eq. (3.23) and illustrates more complex soliton dynamics. This solution, as compared to the earlier figures, shows an asymmetric wave profile in 3D and illustrates the effect of higher-order dispersion or cross-nonlinearities. The contour map illustrates a less localized but coherent wave packet. The 2D slices witness temporal evolution of the waveform with periodic oscillations that exhibit a trade-off between perturbation effects and soliton stability.

The slight asymmetry and weaker localization point to a larger dispersive contribution relative to the nonlinear terms. Small oscillatory features in the flanks are consistent with mixed-derivative effects (through θ) and transverse coupling, which promote weak radiative tails rather than a perfectly compact profile. Nevertheless, the bounded oscillations in the temporal slices indicate metastable persistence of the waveform within the sampled window, without secular growth or drift.

Together, these graphical observations provide evidence for the existence and richness of soliton solutions of the investigated model. They show how changes in parameters lead to varying waveform behavior, including stable solitary pulses, breathing mode, or the dispersive phenomenon, to create the richness of the solution space.

Apart from its soliton behavior, the Boussinesq-type KdV equation further possesses richer complex dynamical phenomena when studied through a reduced system. In the following section, the qualitative dynamics and bifurcation characteristics of the system are explored through tools of nonlinear dynamics.

5. Bifurcation structure and qualitative dynamics of the reduced system

5.1. Derivation of the reduced system

Bifurcation analysis aids in determining whether or not the underlying dynamical system depends on the values of the involved parameters. The Galilean transformation applied to Eq. (3.2) yields the following planar dynamical system:

$$\begin{cases} \dfrac{d\Phi}{d\xi} = T, \\ \dfrac{dT}{d\xi} = w_1\Phi + w_2\Phi^2, \end{cases} \tag{5.1}$$

where $w_1 = -\frac{k(dm+fn+\theta l)+k^2+n^2}{\gamma k^4}$ and $w_2 = -\frac{\lambda}{\gamma k^2}$.

The Hamiltonian is given by:

$$S(\Phi, T) = \frac{T^2}{2} + w_1\frac{\Phi^2}{2} + w_2\frac{\Phi^3}{3} = s, \tag{5.2}$$

where the Hamiltonian constant is denoted by s. The bifurcations of the system (5.1) phase-portraits throughout the parameter space of w_1 and w_2 will now be investigated. The following results can be seen through qualitative analysis.

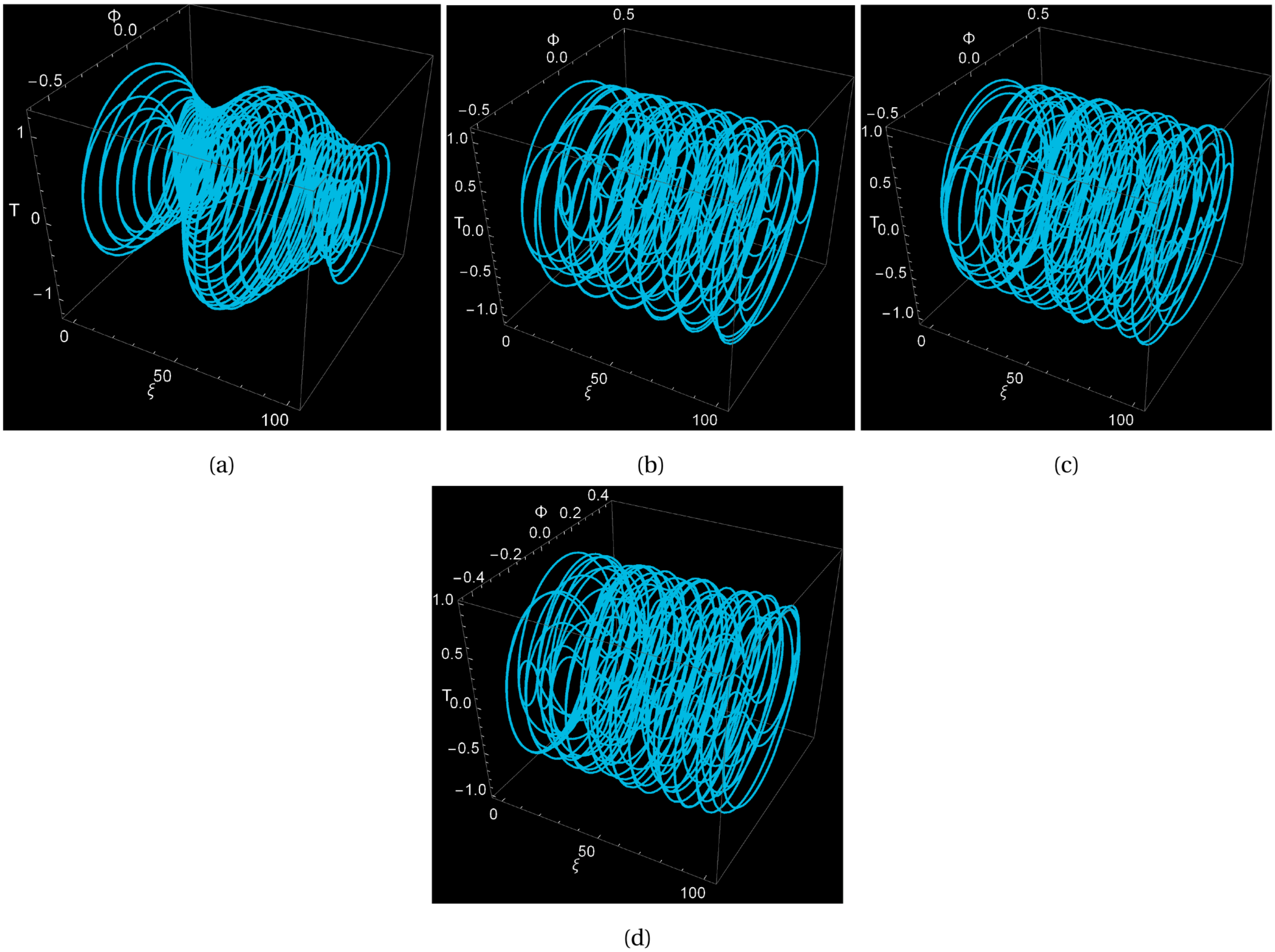

Fig. 10. 3D chaotic analysis of the perturbed system (6.1) using the values $k=1$, $d=0$, $m=0.15$, $f=0.1$, $n=1.196$, $l=0.5$, $\theta=0.4$, $\gamma=-1.1$, $\lambda=-1.65$, $f_0=1.25$, and **a.)** $\delta=3.25$, **b.)** $\delta=3.50$, **c.)** $\delta=3.75$, **d.)** $\delta=4.00$ with the initial condition $(\Phi(0),T(0))=(0.29,0.13)$.

5.2. Equilibrium points and Jacobian analysis

The first thing to note is that system (5.1) has two equilibrium points, which are as follows:

$$\mathcal{G}_1=(0,0) \quad \text{and} \quad \mathcal{G}_2=\left(\frac{-w_1}{w_2},0\right).$$

The Jacobian of (5.1) will be:

$$J(\Phi,T)=\det\begin{vmatrix} 0 & 1 \\ w_1+2w_2\Phi & 0 \end{vmatrix}=-w_1-2w_2\Phi.$$

Therefore, with regard to $J(\Phi,T)<0$, the pair (Φ,T) can be designated as the saddle point. Additionally, it would be a cuspidal for $J(\Phi,T)=0$ and the center for $J(\Phi,T)>0$. By altering the parameter ranges, the intended outcomes can be obtained.

5.3. Phase-portrait analysis under parameter variations

CASE 1: $w_1>0, w_2>0$

For the system (5.1), represented as $\mathcal{G}_1=(0,0)$ and $\mathcal{G}_2=(-1,0)$, as indicated in Fig. 4(a), we have successfully identified two stable points of equilibrium using the values $w_1=1$ and $w_2=1$. Both the center point characteristic of $\mathcal{G}_2$ and the saddle point characteristic of $\mathcal{G}_1$ are readily apparent.

CASE 2: $w_1>0, w_2<0$

The system (5.1) has two critical points for values of $w_1=1$ and $w_2=-1$, namely $\mathcal{G}_1=(0,0)$ and $\mathcal{G}_2=(1,0)$, as shown in Fig. 4(b). When we look more closely, we can see that $\mathcal{G}_1$ is a saddle point, while $\mathcal{G}_2$ is the center.

CASE 3: $w_1<0, w_2<0$

We have successfully extracted the equilibrium points $\mathcal{G}_1=(0,0)$ and $\mathcal{G}_2=(-1,0)$ from the system (5.1) shown in Fig. 4(c) by using the values $w_1=-1$ and $w_2=-1$. It is clear by looking at the phase-portrait that $\mathcal{G}_1$ behaves like a center point, while $\mathcal{G}_2$ takes on the traits of a saddle.

CASE 4: $w_1<0, w_2>0$

The system (5.1) shows two equilibrium points for the values $w_1=-1$ and $w_2=1$, namely $\mathcal{G}_1=(0,0)$ and $\mathcal{G}_2=(1,0)$, as shown in Fig. 4(d). $\mathcal{G}_1$ is clearly a center point, and $\mathcal{G}_2$ is clearly the saddle.

CASE 5: $w_1=0, w_2\neq 0$

Only a single point of equilibrium, $\mathcal{G}_1=(0,0)$, can be discovered for $w_1=0$ and $w_2=-1$, as shown in the example in Fig. 4(e). By analyzing the Jacobian, it has been established that $\mathcal{G}_1$ behaves in a cusp manner.

The bifurcation analysis reveals how the system's fixed points and stability evolve with changing parameters. To explore the system's response to external periodic perturbations, we now extend our analysis to include chaotic dynamics and sensitivity studies.

6. Chaotic behavior and sensitivity analysis

6.1. Formulation of the perturbed system

Using the previously mentioned planar dynamical system in Eq. (5.1), we add the perturbation term $f_0\cos(R)$ to investigate the dis-

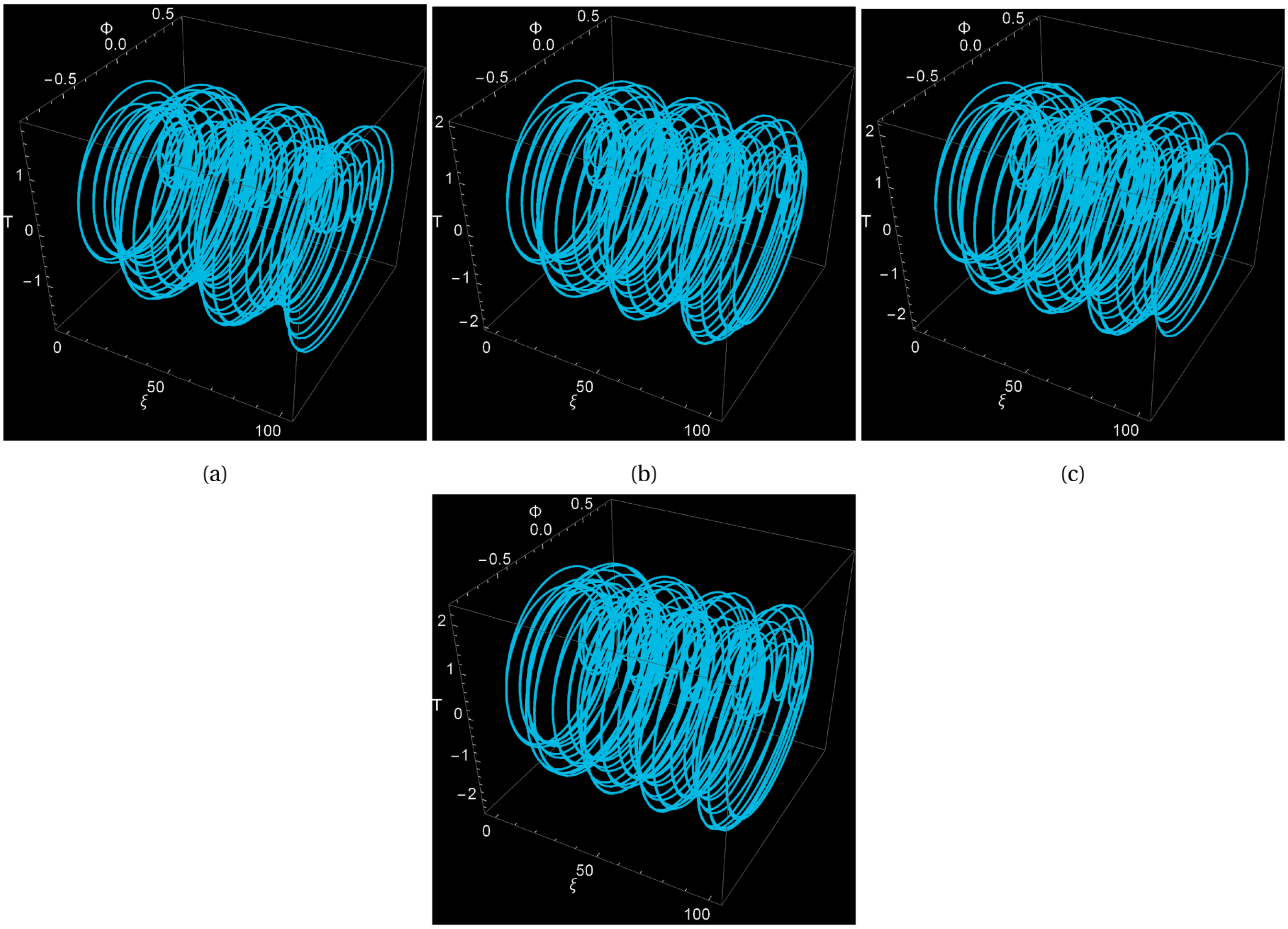

(a) (b) (c)

(d)

Fig. 11. 3D chaotic analysis of the perturbed system (6.1) using the values $k = 1$, $d = 0$, $m = 0.15$, $f = 0.1$, $n = 1.196$, $l = 0.5$, $\theta = 0.4$, $\gamma = -1.1$, $\lambda = -1.65$, $\delta = 3.25$, and **a.)** $f_0 = 2.25$, **b.)** $f_0 = 2.50$, **c.)** $f_0 = 2.75$, **d.)** $f_0 = 3.00$ with the initial condition $(\Phi(0), T(0)) = (0.29, 0.13)$.

ordered resolution of Eq. (3.2). Thus, we obtain:

$$\begin{cases} \dfrac{d\Phi}{d\xi} = T, \\ \dfrac{dT}{d\xi} = w_1\Phi + w_2\Phi^2 + f_0\cos(R), \\ \dfrac{dR}{d\xi} = \delta, \end{cases} \tag{6.1}$$

where $R = \delta\xi$. The amplitude and frequency of the external force applied to the system (6.1) are represented by the parameters f_0 and δ in the given system. In the present work, we investigate the effect of the perturbation parameters $f_0\cos(R)$ on the planar dynamical system (6.1). The influence of outside factors may lead a system to act in a random and unpredictable manner. We found this specific phenomenon in system (6.1), which is chaotic in movement in our work, whose trajectories change over time and exhibit divergences from regular patterns.

There are other methods for detecting chaos; however, in this academic paper, we will focus on the most useful ones:

- Bifurcation Diagram,
- Sensitivity to Frequency and Amplitude,
- Chaotic Analysis,
- Poincaré Map,
- Time Series.

6.2. Bifurcation diagrams and transition to chaos

A bifurcation diagram is a powerful visualization tool for watching the qualitative behavior of a dynamical system when a system parameter varies. It typically graphs the asymptotic state of a state variable, for example, fixed points or periodic orbits, against the bifurcation parameter, and indicates such critical transitions as the onset of chaos, period-doubling, and other dynamical instabilities. We consider, in the current paper, the bifurcation diagram of the perturbed chaotic system (6.1) and observe how the changes of the bifurcation parameter affect the long-term dynamics of the state variable Φ, as shown in Fig. 5.

From a physical perspective, such bifurcation scenarios tell us that the interaction of linear and nonlinear terms in the dynamical system controls the nature and stability of wave-like structures in the underlying medium. The center-type equilibria correlate with bounded stable wave profiles, while saddle points signify unstable directions and potential evolution towards higher-order dynamics. Cusp behavior implies critical thresholds at which minute perturbations may profoundly modify the evolution of the system. This analysis provides a fundamental understanding of the impact of structural changes in the parameter space on the global dynamics of the system, setting the stage for further exploration of chaotic dynamics under the influence of external perturbations. Furthermore, bifurcation diagrams not only map the stability topography of a system but also help identify parameter boundaries that lead to extreme behavior changes. These critical points are especially useful to

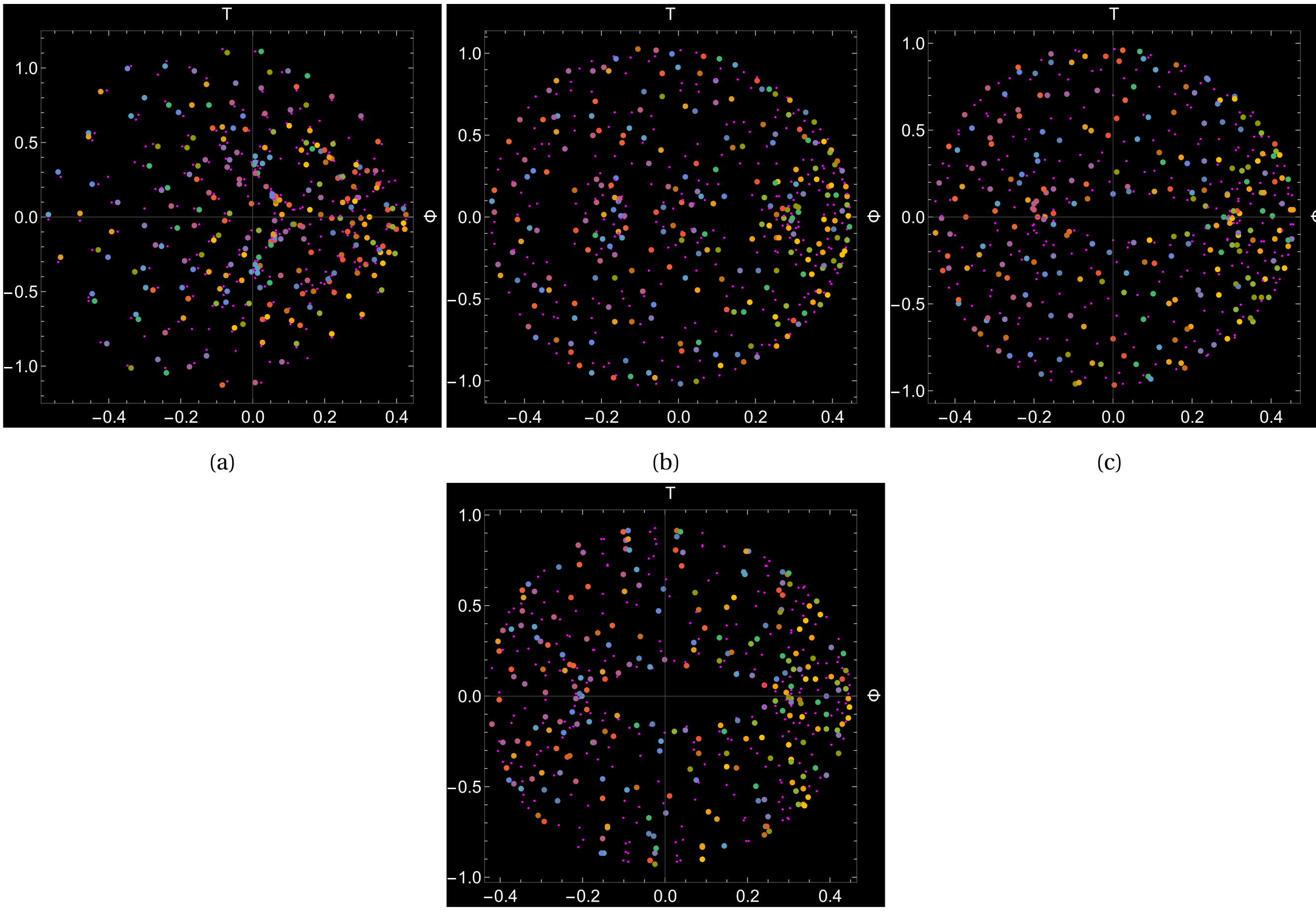

(a) (b) (c)

(d)

Fig. 12. Poincaré maps of the perturbed system (6.1) using the values $k = 1$, $d = 0$, $m = 0.15$, $f = 0.1$, $n = 1.196$, $l = 0.5$, $\theta = 0.4$, $\gamma = -1.1$, $\lambda = -1.65$, $f_0 = 1.25$, and **a.)** $\delta = 3.25$, **b.)** $\delta = 3.50$, **c.)** $\delta = 3.75$, **d.)** $\delta = 4.00$ with the initial condition $(\Phi(0), T(0)) = (0.29, 0.13)$.

employ in applications where the system behavior must be controlled to high precision, such as in mechanical oscillators, power grids, or laser devices.

The bifurcation diagram plotted in Fig. 5 illustrates how the system state variable T (the derivative of the wave profile Φ) varies as a function of the bifurcation parameter ζ. Physically, ζ might be a control parameter such as the amplitude or frequency of a periodic forcing input to the system. For lower values of $\zeta \in [0.6, 0.9]$, the system shows one smooth curve for T, indicating periodic and stable dynamics. However, as ζ approaches some critical value, the graph shows a sudden and tremendous jump in the values of T, indicating an abrupt switch in the dynamics of the system. This bifurcation marks the beginning of complicated, perhaps chaotic behavior, in which tiny changes in ζ result in large and uncontrollable changes in the state variable. Physically, it means that the system is very sensitive to external stimuli and its dynamics are no longer controlled by periodic oscillations but by non-periodic, aperiodic motion that is typical of chaotic dynamics. This kind of bifurcation dynamics plays a crucial role in investigating the order-to-chaos transition in nonlinear wave systems driven by external perturbations.

6.3. Sensitivity to frequency and amplitude

The sensitivity analysis in Figs. 6 and 7 shows that slight changes in the parameters δ and f_0, the frequency and amplitude of the external forcing term $f_0 \cos(R)$, respectively, can have a large effect on the chaotic behavior of the system.

In Fig. 6, we hold $f_0 = 1.25$ constant and change the frequency parameter δ. As δ varies from 3.25 to 4.00, we can see that orbits in the (Φ, T) phase space become increasingly irregular and more spread out. This indicates a trend towards more intense chaotic dynamics as the frequency of the external drive is turned up. Physically, this implies that the system is more sensitive to high-frequency disturbances and therefore develops more intricate and less predictable patterns of motion.

Likewise, in Fig. 7, the frequency δ is kept fixed at 3.25 while the forcing amplitude f_0 is changed between 2.25 and 3.00. The graphs show that by making f_0 larger, the oscillations are bigger and chaotic fluctuations are more intense. This illustrates that larger forcing amplitudes strengthen the instability of the system. The trajectory density and dispersion are greater, which corresponds to a more energetic and disordered dynamical state. This is the way in which the stronger external force pumps more energy into the system and amplifies its random response.

These findings define the frequency and amplitude responsiveness of the perturbed nonlinear system. Practically, this kind of response has implications in the engineering aspect of stability in systems or in the modeling of phenomena in plasma physics and fluid dynamics, where even infinitesimally small periodic perturbations can lead to complicated, unpredictable dynamics.

6.4. Chaotic analysis (2D and 3D)

A phase-portrait is a fundamental graphical tool that maps the orbits of a dynamical system in the phase (or state) space, which tells us how

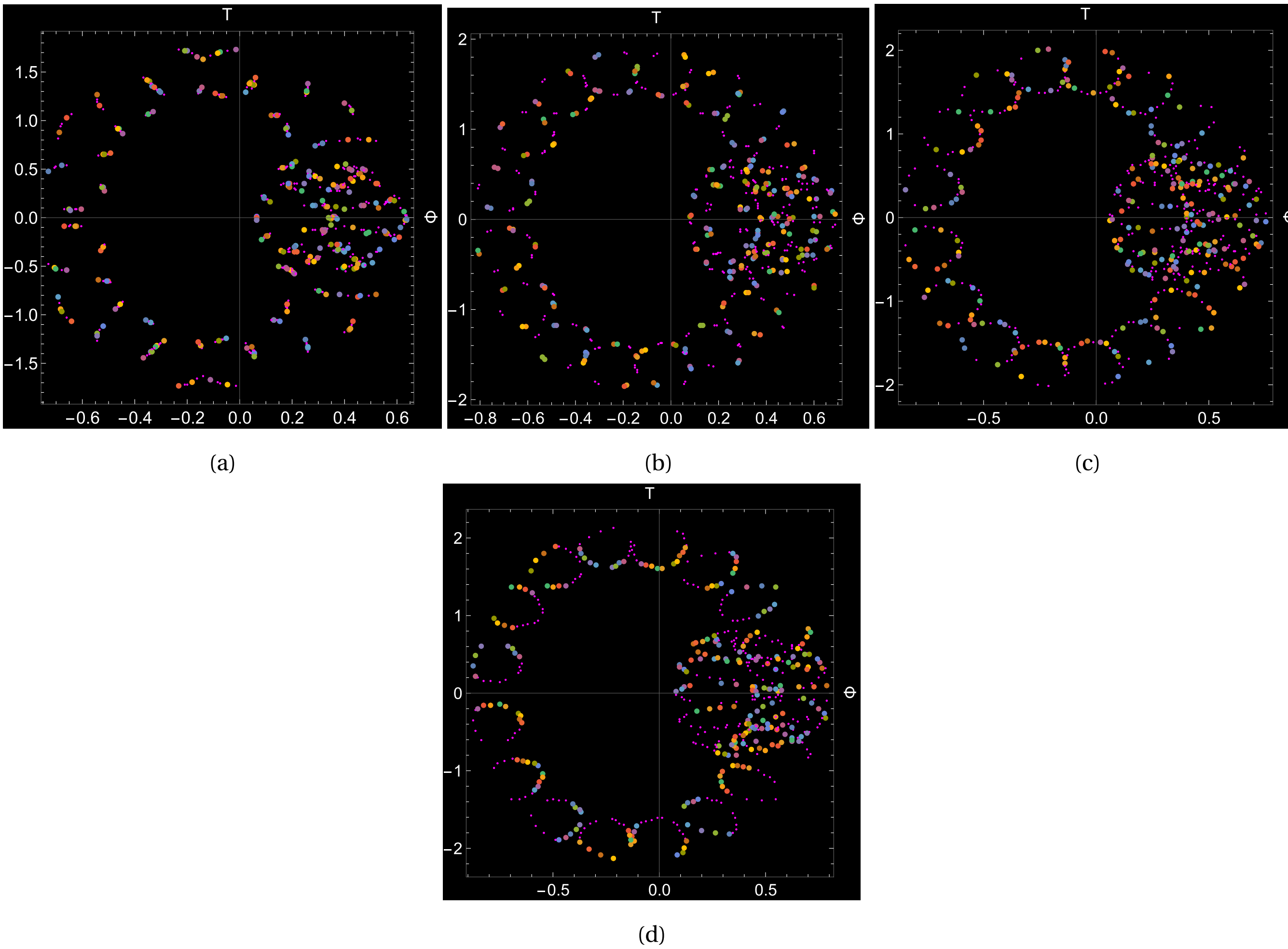

Fig. 13. Poincaré maps of the perturbed system (6.1) using the values $k = 1$, $d = 0$, $m = 0.15$, $f = 0.1$, $n = 1.196$, $l = 0.5$, $\theta = 0.4$, $\gamma = -1.1$, $\lambda = -1.65$, $\delta = 3.25$, and **a.)** $f_0 = 2.25$, **b.)** $f_0 = 2.50$, **c.)** $f_0 = 2.75$, **d.)** $f_0 = 3.00$ with the initial condition $(\Phi(0), T(0)) = (0.29, 0.13)$.

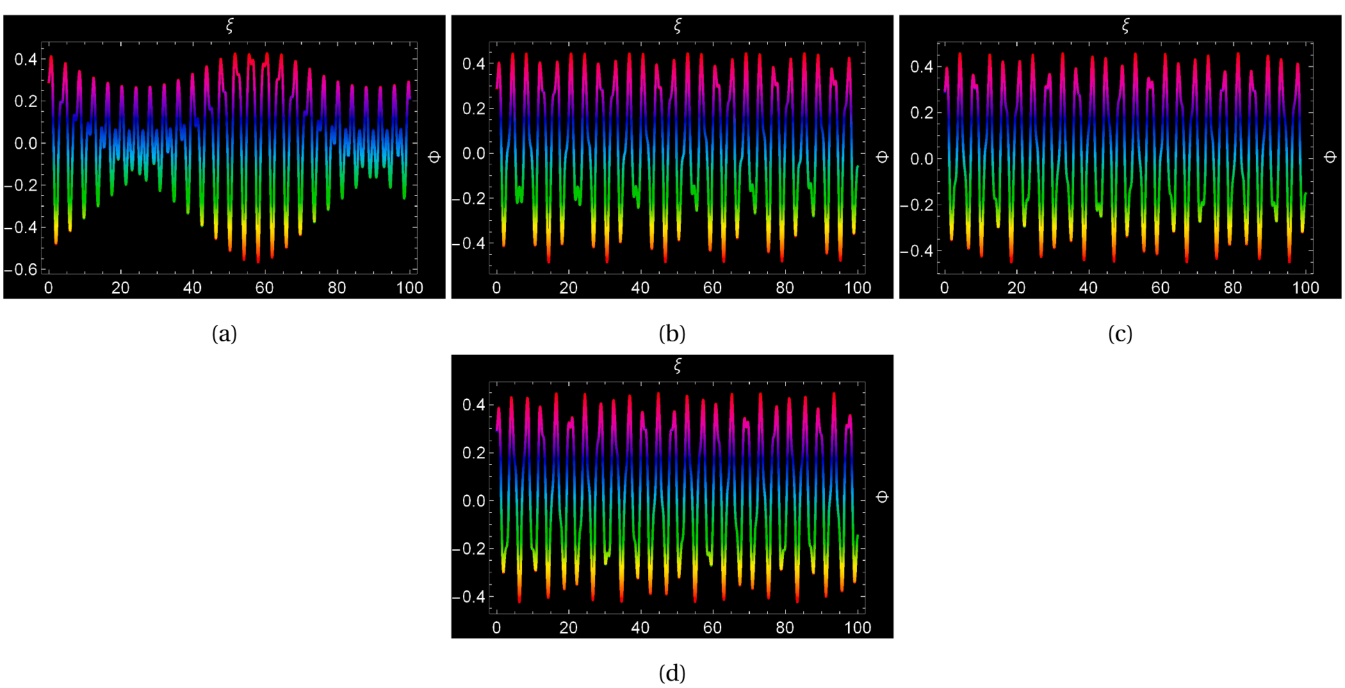

Fig. 14. Time series of the perturbed system (6.1) using the values $k = 1$, $d = 0$, $m = 0.15$, $f = 0.1$, $n = 1.196$, $l = 0.5$, $\theta = 0.4$, $\gamma = -1.1$, $\lambda = -1.65$, $f_0 = 1.25$, and **a.)** $\delta = 3.25$, **b.)** $\delta = 3.50$, **c.)** $\delta = 3.75$, **d.)** $\delta = 4.00$ with the initial condition $(\Phi(0), T(0)) = (0.29, 0.13)$.

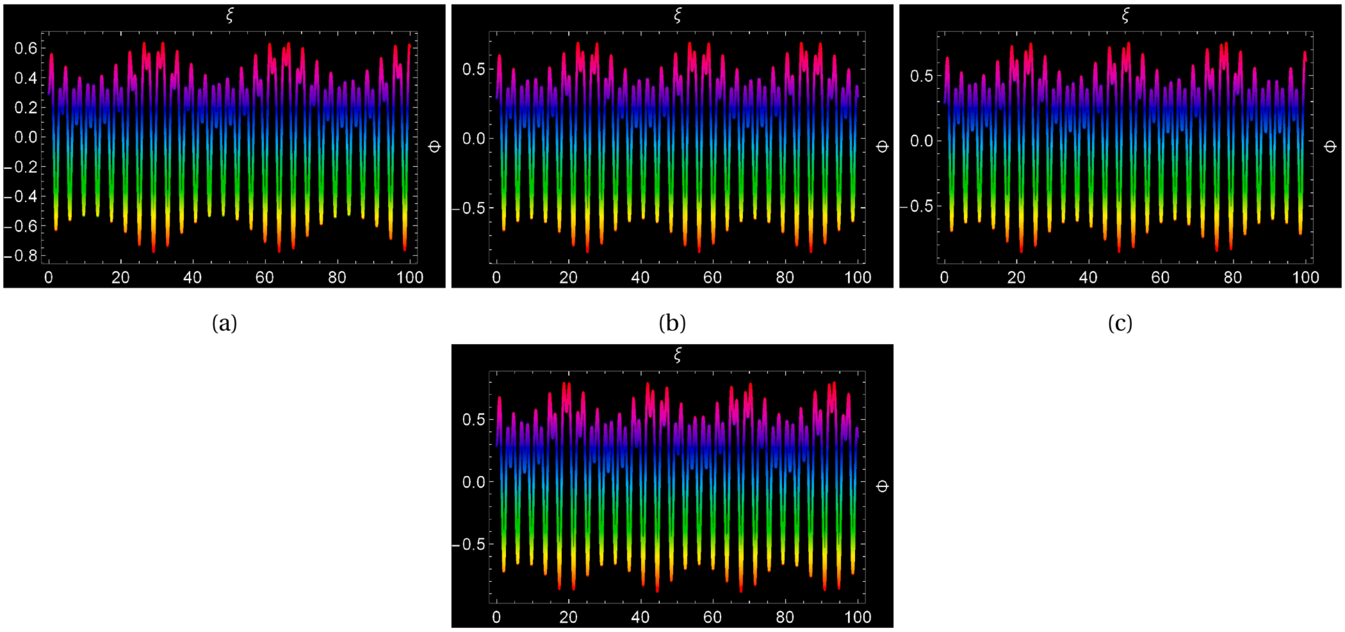

Fig. 15. Time series of the perturbed system (6.1) using the values $k = 1$, $d = 0$, $m = 0.15$, $f = 0.1$, $n = 1.196$, $l = 0.5$, $\theta = 0.4$, $\gamma = -1.1$, $\lambda = -1.65$, $\delta = 3.25$, and **a.)** $f_0 = 2.25$, **b.)** $f_0 = 2.50$, **c.)** $f_0 = 2.75$, **d.)** $f_0 = 3.00$ with the initial condition $(\Phi(0), T(0)) = (0.29, 0.13)$.

the system develops over time from various starting conditions. The portraits enable us to disclose the qualitative behavior and stability of the system, such as aspects like fixed points, limit cycles, and chaotic attractors. For the perturbed planar system (6.1), we study the trajectory evolution in the (Φ, T) plane to investigate the system response under various external forcing conditions, as given in Figs. 8 to 11.

Figs. 8 and 9 are the two-dimensional phase-portraits of the system for changing values of the frequency parameter δ and forcing amplitude f_0, respectively. In Fig. 8, f_0 is kept constant while δ is changed from 3.25 to 4.00. We observe that with higher frequency, orbits are more chaotic and dispersed in the phase space, depicting the onset of more intense chaotic dynamics. The loss of symmetry and periodicity in the orbits is characteristic of the increasing sensitivity of the system to external oscillations. In Fig. 9, however, δ is held constant and the forcing amplitude f_0 is varied. The graphs clearly reveal that a larger f_0 injects more energy into the system, and the orbits become more complex and dispersed. This behavior confirms the fact that the amplitude growth of external excitation strengthens the chaotic character of the response, destabilizing periodic or quasi-periodic motion.

In addition to the 2D plots, Figs. 10 and 11 display the corresponding three-dimensional phase-portraits with the variable $R = \delta\xi$ varying linearly with time. The 3D plots show more of the system's fine-scale evolution, with curved and dense sets of orbits spiraling and folding into each other–characteristics of chaotic attractors. Three-dimensional geometry still maintains the internal dynamics-external forcing dependence.

Physically, the phase-portraits highlight the nonlinear system's tendency to evolve from regular to chaotic behavior with increasing excitation. Such behaviors are especially crucial in wave mechanics, electrical circuitry, and plasma physics systems in which periodic forces applied from the outside can lead to resonance or instability. By studying the geometry of such trajectories, one not only establishes the stability of solutions but also determines the level of predictability and sensitivity embedded into the dynamics.

These phase-portraits serve as visual confirmations of chaos and complement the analytical and numerical techniques used throughout the study.

The obtained analytical wave solutions are validated by the qualitative structures evident in the phase-portraits. That is, the trigonometric and hyperbolic soliton solutions are associated with near-elliptic or closed orbits around stable centers as a symbol of bounded solitary or periodic propagation. The exponential and rational-type solutions, however, are associated with open or divergent orbits as a symbol of unbounded or unstable behavior in the phase space. Thus, the transformation from periodic regular routes to random chaotic trajectories in the portraits is visually observed to represent the loss of stability and modulation of the analytical solutions under the influence of external excitation.

Although phase-portraits provide continuous information about the structure of the system's orbits, they become messy in chaotic regimes. To prevent this and achieve cleaner patterns, we now turn to the Poincaré map, a discrete sampling method providing a clearer picture of the long-term dynamics.

6.5. *Poincaré map analysis*

The Poincaré map is an important tool of nonlinear dynamics that reduces the dimension of a system of continuous time by sampling discretely the state of the system at equally spaced times or whenever the trajectory crosses some specified lower-dimensional surface, referred to as the Poincaré section. This technique is valuable for chaos detection and characterization of chaotic behavior because it unwinds periodic or quasi-periodic orbits and renders patterns visible that might be hidden in the full continuous trajectory. The chaos detection behavior of the Poincaré map is illustrated in Figs. 12 and 13.

These are the Poincaré sections of the perturbed dynamical system (6.1) with changing parameter conditions. In Fig. 12, the forcing amplitude f_0 is kept fixed while the frequency parameter δ is changed. As δ increases from 3.25 to 4.00, the structure of the Poincaré plots changes from regular to increasingly scattered and more random point clouds. This shift initiates and strengthens chaos when the orbits do not come back to points regularly but instead produce a crowded set of non-periodic intersections.

Fig. 13 demonstrates the opposite scenario: δ is constant and f_0 is amplified. The plots indicate that higher amplitudes of external driving produce more complex and more chaotic intersections on the Poincaré section. At a lower f_0, the points may create visible closed loops hinting at quasi-periodic orbits. As f_0 increases, these loops turn into stochastic-like scatters, indicating a full chaotic situation. The evolution from order to chaos through bifurcations is nicely represented by this discrete dynamical model.

Physically, the Poincaré map illustrates the way periodic forcing influences the system's internal dynamics. First, systems that respond periodically or quasi-periodically may lose predictability as there is more or more rapid excitation. In engineering, physics, and biological systems, such behavior is equivalent to a loss of synchronization, the onset of turbulence, or signal transfer instability.

The advantage of the Poincaré map is that it reduces complex, high-dimensional flows to two-dimensional patterns that are simpler to classify. It provides a fingerprint of long-term dynamics in the system and serves as a diagnostic tool for confirming chaotic regimes predicted by phase-portrait and bifurcation analysis.

6.6. Time series behavior

Time series analysis is a standard analysis method of nonlinear dynamical systems, in which a time series is an array of data points at later and later times. In system (6.1), the time series gives the time evolution of a state variable, for example, Φ, and shows the temporal behavior, stability, periodicity, and potential chaotic behavior of the system. The time series plots in Figs. 14 and 15 illustrate the chaotic behavior of the system in different regimes of parameters.

On these plots, time series of Φ are shown for different values of the frequency parameter δ and forcing amplitude f_0, respectively. In Fig. 14, f_0 is constant and δ is changed from 3.25 to 4.00. For small values of δ, the system shows reasonably periodic oscillatory behavior. However, the more δ is increased, the less periodic are the oscillations with no apparent periodic structure. This loss of periodicity signals the onset of ordered-to-chaotic behavior as the system is driven at higher frequencies.

Fig. 15, δ is fixed and the amplitude f_0 is increased from 2.25 to 3.00. The resulting time series indicates a similar transition: low values of f_0 produce nearly periodic signals, while higher amplitudes lead to erratic fluctuations with rapidly changing amplitudes. These irregular time-domain signatures are characteristic of chaotic systems, where the long-term evolution becomes highly sensitive to initial conditions and parameter variations.

From a physical perspective, the time series provides a direct view into the temporal complexity of the system. In real-world applications such as fluid flow, wave propagation, or plasma dynamics, these signals might represent measurable quantities like velocity, pressure, or electric field intensity. The emergence of chaotic fluctuations in the time series implies unpredictability and a breakdown of regular behavior, which are important considerations for stability, control, and energy distribution in applied systems.

The time series plots, when interpreted together with bifurcation diagrams, phase-portraits, and Poincaré maps, give a consistent and comprehensive account of the nonlinear dynamics. They establish chaos existence and further show how the interaction between forcing parameters governs the order-disorder transition.

Overall, the marriage of time series analysis to bifurcation, phase space visualization, and discrete mapping techniques provides a strong and complete picture of the system's nonlinear nature. These multiple windows of analysis corroborate the evidence of the existence of chaos and its sensitivity to external excitation parameters.

7. Conclusion

Herein, we studied a newly extended Boussinesq-type KdV equation with the higher-order and mixed partial derivatives pertinent to multidimensional nonlinear wave propagation. We obtained systematically a large class of exact solutions, including Jacobi elliptic function, trigonometric, hyperbolic, and exponential forms, using the Kumar-Malik method, an efficient and handy approach for solving nonlinear partial differential equations. These solutions provide excellent insight into the rich dynamics of the provided equation and reveal how different selections of parameters affect the wave profile, leading to solitons, breathers, and localized pulses.

In order to learn yet more about the qualitative behavior of the system, we studied the corresponding reduced planar dynamical system derived from the original equation by a Galilean transformation. From bifurcation and phase- portrait analysis, we had already determined system parameter-controlled dynamics transitions and equilibrium configurations. With further inclusion of the external perturbations, we could identify chaotic dynamics, the analysis of which we performed using sensitivity, bifurcation diagrams, and phase-portraits. These diagnostics had confirmed the system's sensitivity to small forcing frequency and amplitude changes characteristic of chaotic dynamics.

This paper appears to be the initial application of Kumar-Malik method to this specific Boussinesq-type KdV model and the initial combined analytical and dynamical analysis of its solutions. What is learned here not only goes deeper into the theoretical foundation of extended KdV-type equations but also introduces useful tools in exploring wave phenomena in fluid mechanics, plasma physics, and nonlinear optics.

In future work, the present framework could be extended to the non-autonomous form of the model, where variable coefficients may lead to richer dynamical transitions and modulation phenomena. Besides, follow-up research will encompass the numerical checking of the acquired solutions, the enlargement of the study to variable-coefficient or fractional-order systems, and the experimental or computational investigations of the resonance and stability behaviors.

CRediT authorship contribution statement

Mehmet Şenol: Writing - original draft, Visualization, Validation; **Bahadır Kopçasız:** Project administration, Methodology, Investigation; **Hatice Ceyda Türk:** Writing - review & editing, Supervision, Software; **Homan Emadifar:** Formal analysis, Data curation, Conceptualization; **Karim K. Ahmed:** Validation, Resources, Formal analysis.

Data availability

No data was used for the research described in the article.

Declaration of competing interest

The authors declare that they have no known competing financial interests or personal relationships that could have appeared to influence the work reported in this paper.

Acknowledgments

Not applicable.

References

[1] K.K. Ahmed, H.M. Ahmed, N.M. Badra, M. Mirzazadeh, W.B. Rabie, M. Eslami, Diverse exact solutions to Davey-Stewartson model using modified extended mapping method. Nonlinear Anal. Model. Contr., 29, 2024.
[2] P.G. Drazin, R.S. Johnson, Solitons: An Introduction, Cambridge University Press, 1989.
[3] G.B. Whitham, Linear and Nonlinear Waves, Wiley, 1974.
[4] H.H. Hussein, K.K. Ahmed, H.M. Ahmed, A. Elsheikh, W. Alexan, Existence of novel analytical soliton solutions in a magneto-electro-elastic annular bar for the longitudinal wave equation. Opt. Quant. Electron., 56, 2024.
[5] D.J. Korteweg, G.D. Vries, On the change of form of long waves advancing in a rectangular canal, and on a new type of long stationary waves, Philos. Mag. 39 (5) (1895) 422443.
[6] D.H. Peregrine, Long waves on a beach, J. Fluid Mech. 27 (4) (1967) 827.

[7] A. Yildirim, An algorithm for solving the Boussinesq equation using the adomian decomposition method, J. Comput. Appl. Math. 217 (1) (2009) 43. https://doi.org/10.1016/j.cam.2007.05.019
[8] Y. Kai, S. Chen, K. Zhang, Z. Yin, A study of the shallow water waves with some boussinesq-type equations, Waves Rand. Complex Med. 34 (3) (2024) 1251–1268.
[9] H.F. Ismael, T.A. Sulaiman, U. Younas, H.R. Nabi, On the autonomous multiple wave solutions and hybrid phenomena to a (3 1)-dimensional Boussinesq-type equation in fluid mediums, Chaos Solitons Fract. 187 (2024) 115374.
[10] C. Chen, M. Li, Families of exact solutions ogeneralized (2 1)-dimensional Boussinesq type equation, Wave Motion 127 (2024) 103297.
[11] A.R. Seadawy, H. Zahed, M. Iqbal, Solitary wave solutions for the higher dimensional Jimo-Miwa dynamical equation via new mathematical techniques, Mathematics 10 (7) (2022) 1011.
[12] M. Iqbal, A.R. Seadawy, O.H. Khalil, D. Lu, Propagation of long internal waves in density stratified ocean for the (2 1)-dimensional nonlinear Nizhnik-Novikov-Vesselov dynamical equation, Results Phys. 16 (2020) 102838.
[13] W.A. Faridi, M.A. Bakar, A. Jhangeer, F. Tawfiq, R. Myrzakulov, A. Naizagarayeva, The generalized soliton wave structures and propagation visualization for Akbota equation, Zeitschrift für Naturforschung A 79 (12) (2024) 1075–1091.
[14] A. Saboor, M. Shakeel, X. Liu, A. Zafar, M. Ashraf, A comparative study of two fractional nonlinear optical model via modified G'^2-expansion method, Opt. Quant. Electron. 56 (2) (2024) 259.
[15] B. Ghanbari, C.K. Kuo, New exact wave solutions of the variable-coefficient (1 1)-dimensional Benjamin-Bona-Mahony and (2 1)-dimensional asymmetric Nizhnik-Novikov-Veselov equations via the generalized exponential rational function method, Eur. Phys. J. Plus 134 (7) (2019) 334.
[16] B. Ghanbari, J.G. Liu, Exact solitary wave solutions to the (2 1)-dimensional generalised Camassa-Holm-Kadomtsev-Petviashvili equation, Pramana 94 (1) (2020) 21.
[17] F.U. Afrin, Solitary wave solutions and investigation the effects of different wave velocities of the nonlinear modified Zakharov Kuznetsov model for the wave propagation in nonlinear media, Partial Differ. Equ. Appl. Math. 8 (2023) 100583.
[18] M.N. Islam, M. Al-Amin, M.A. Akbar, Abundant closed-form solitary solutions of a nonlinear neurobiological model for analyzing numerous signal transmission behaviors through the neuron using recent scheme, Partial Differ. Equ. Appl. Math. 13 (2025) 101051.
[19] A.H. Arnous, M. Mirzazadeh, L. Akinyemi, A. Akbulut, New solitary waves and exact solutions for the fifth-order nonlinear wave equation using two integration techniques, J. Ocean Eng. Sci. 8 (5) (2023) 475–480.
[20] M.M.A. El-Sheikh, H.M. Ahmed, A.H. Arnous, W.B. Rabie, A. Biswas, A.S. Alshomrani, M.R. Belic, Optical solitons in birefringent fibers with Lakshmanan Porsezian Daniel model by modified simple equation, Optik 192 (2019) 162899.
[21] A. Jhangeer, W.A. Faridi, M. Alshehri, Soliton wave profiles and dynamical analysis of fractional ivancevic option pricing model, Sci. Rep. 14 (1) (2024) 23804.
[22] M.I. Afridi, M.A.S. Murad, W.A. Faridi, M. Iqbal, F. Tawfiq, A.H. Arnous, The fractional solitary wave profiles and dynamical insights with chaos analysis and sensitivity demonstration, Results Phys. 65 (2024) 107971.
[23] M. Shakeel, X. Liu, A. Al-Yaari, Interaction of lump, periodic, bright and kink soliton solutions of the (1 1)-dimensional Boussinesq equation using Hirota-bilinear approach, J. Nonlinear Math. Phys. 31 (1) (2024) 1–18.
[24] Z. Zhang, W. Li, B. Li, Perturbation of plane waves for the fourth-order defocusing Schrödinger equation, Phys. Scr. 100 (9) (2025) 095221.
[25] Z. Zhang, Y. Chen, W. Li, F. Li, X. Yang, B. Li, Slowly varying solitary waves in the extended shallow water model with a perturbation term, Phys. Scr. 100 (2) (2025) 025214.
[26] D.V. Tanwar, A.M. Wazwaz, Lie symmetries, optimal system and dynamics of exact solutions of (2 1)-dimensional KP-BBM equation, Phys. Scr. 95 (6) (2020) 065220.
[27] D.V. Tanwar, Optimal system, symmetry reductions and group-invariant solutions of (2 1)-dimensional ZK-BBM equation, Phys. Scr. 96 (6) (2021) 065215.
[28] D.V. Tanwar, A.M. Wazwaz, Lie symmetries and exact solutions of KdV-Burgers equation with dissipation in dusty plasma, Qual. Theory Dyn. Syst. 21 (4) (2022) 164.
[29] D.V. Tanwar, P.K. Sahu, Dynamics of one-dimensional motion of a gas under the influence of monochromatic radiation, Qual. Theory Dyn. Syst. 22 (2) (2023) 54.
[30] M. Kumar, D.V. Tanwar, On lie symmetries and invariant solutions of (2 1)-dimensional Gardner equation, Commun. Nonlinear Sci. Numer. Simul. 69 (2019) 45–57.
[31] D.V. Tanwar, M. Kumar, Lie symmetries, exact solutions and conservation laws of the Date-Jimbo-Kashiwara-Miwa equation, Nonlinear Dyn. 106 (4) (2021) 3453–3468.
[32] D.V. Tanwar, A.M. Wazwaz, Lie symmetries and dynamics of exact solutions of dissipative Zabolotskaya-Khokhlov equation in nonlinear acoustics, Eur. Phys. J. Plus 135 (6) (2020) 520.
[33] D.V. Tanwar, Lie symmetry reductions and generalized exact solutions of Date-Jimbo-Kashiwara-Miwa equation, Chaos Solitons Fract. 162 (2022) 112414.
[34] D.V. Tanwar, R. Kumar, A novel class of soliton solutions and conservation laws of the generalised BS equation by lie symmetry method, Pramana 98 (3) (2024) 113.
[35] Anukriti, D.V. Tanwar, Lie symmetry reductions and exact solutions of Kadomtsev-Petviashvili equation, Pramana 99 (1) (2025) 35.
[36] S. Roy, S. Raut, R.R. Kairi, P. Chatterjee, Bilinear Bäcklund, Lax pairs, breather waves, lump waves and soliton interaction of (2 1)-dimensional non-autonomous Kadomtsev-Petviashvili equation, Nonlinear Dyn. 111 (6) (2023) 5721–5741.
[37] U. Ghosh, S. Roy, S. Biswas, S. Raut, A non-autonomous fractional granular model: multi-shock, breather, periodic, hybrid solutions and soliton interactions, Chaos Solitons Fract. 187 (2024) 115393.
[38] S. Biswas, U. Ghosh, S. Raut, Construction of fractional granular model and bright, dark, lump, breather types soliton solutions using hirota bilinear method, Chaos Solitons Fract. 172 (2023) 113520.
[39] W. Alhejaili, S. Roy, S. Raut, A. Roy, A.H. Salas, T. Aboelenen, S.A. El-Tantawy, On the integrability, multi-shocks, high-order kinky-breathers, L-lump-kink solutions for the non-autonomous perturbed potential Kadomtsev-Petviashvili equation, Nonlinear Dyn. 112 (15) (2024) 13335–13359.
[40] S. Roy, R. Barman, S. Raut, On aspect of integrability, soliton, breather and positon solutions for the non-autonomous perturbed Gardner equation via Darboux transformation, Nonlinear Dyn. 113 (14) (2025) 18503–18526.
[41] J. Turi, S. Roy, S. Raut, Modulational instability and dynamics of multidimensional dust ion-acoustic wave envelope in collisional dense astrophysical dusty plasma, Chaos Solitons Fract. 199 (2025) 116696.
[42] H.K. Malik, R. Kumar, An analytical approach to the solution of nonlinear partial differential equations using the modified homotopy perturbation method, J. Appl. Math. 2012, pp. 1–9. https://doi.org/10.1155/2012/645459
[43] A.M. Wazwaz, L. Kaur, New integrable Boussinesq equations of distinct dimensions with diverse variety of soliton solutions, Nonlinear Dyn. 97 (2019) 83–94.
[44] A.M. Wazwaz, S.A. El-Tantawy, L.S. El-Sherif, A.S. Al-Johani, H.A. Alyousef, Multiple soliton and lump solutions to a variety of novel integrable multi-dimensional Boussinesq-type equations, Alexan. Eng. J. 123 (2025) 1–16.
[45] F.N.K. Sağlam, B. Kopçası z, K.U. Tariq, Optical solitons and dynamical structures for the zig-zag optical lattices in quantum physics, Int. J. Theor. Phys. 64 (2) (2025) 1–20.